NUMERICAL SIMULATIONS OF THE FLOW AND PLUGGING BEHAVIOUR OF HYDRATE PARTICLES

Eirik Daniel Fatnes

Master Thesis in Multiphase Systems, Process Technology
Department of Physics and Technology
University of Bergen

May 2010

Abstract

The main hydrate mitigation used by the industry today is to avoid formation at all cost. Avoidance of hydrate formation is made possible by use of inhibitors such as methanol or glycol. These are so called thermodynamic inhibitors which change the thermodynamic conditions of the system to conditions where hydrates cannot be formed. Adding inhibitors while controlling the pressure and temperature is a very costly process.

A new hydrate paradigm is evolving from avoidance of hydrates by inhibition towards risk management. In many situations it is more economical to do risk management of hydrate plugging instead of completely avoiding hydrates. Avoidance is based on thermodynamics, but risk management is based on kinetics. Today's knowledge of hydrate kinetics is not accurate enough to alone be the foundation of risk management. A combination of hydrate kinetics and operating experience must constitute this foundation today.

The purpose of this work was to study the physics of hydrate particle flow in pipelines using numerical simulations. The numerical simulations were performed using ANSYS CFX, and may be compared with simulations performed in another study [1] using STAR-CD for purposes of comparison and clearer interpretation of the physics of bed formation. In general it is important to compare simulations between software packages to destil out which flow features are due to the numerical techniques and which can be assigned to the physics of the system. Results from the numerical simulations for both softwares were compared to experimental results from a multiphase flow loop.

A Eulerian-Eulerian two-fluid model was created using ANSYS CFX. Simulations in a flow regime whereby hydrate deposition was observed during experiments were performed. The apparent viscosity of the hydrate particle suspensions, which was found experimentally to follow one of the published relations for the viscosity of suspensions, was studied. A sensitivity study of the model was done for clarification of the effect of the apparent viscosity and the particle size on the model outcome.

Acknowledgements

This thesis is a part of the HYADES project, which is a collaboration project between SINTEF, Chevron, Statoil and the University of Bergen. The principal objective of this project is to develop a fundamental understanding of hydrate deposition in multiphase transport of petroleum fluids.

The last two years have been very busy but also interesting and very challenging. Combining a full time job as a process engineer in Aibel, masterdegree in multiphase systems and having a little daughter at home, left little time for other activities. During this period I am very grateful for all help, support and encouragement I've got, both from my supervisors, colleagues, friends and family.

First I want to thank professor Alex C. Hoffmann and associated professor Pawel Kosinski for the guidance, advice and support I have received throughout this thesis.

Thanks to PhD. student Boris Balakin who has been very helpful with his knowledge of the experiments conducted prior to this thesis and his help with the CFD simulations. You have always given me quick response on my numerous emails I have sent you. I am very grateful for all your help.

I would also like to thank my employee Aibel for providing the necessary software and for being such a good place to work.

At last I want to give a special thanks to my family, especially Ingeborg and Olan, who are valuable babysitters and did a good job on proofreading this thesis.

A special thanks to my lovely wife Sigrid and my daughter Ingrid. Thank you Sigrid for your support, patience and understanding throughout this thesis. Ingrid, you are my sunshine. Thank you for all the good moments you give me every day.

Thank you!

Contents

Chapter 1

Introduction

In petroleum production the formation of gas hydrate is a major scientific problem since the appearance in pipeline and process equipment can cause cost due to increased pressure loss or even plugging in the system. Gas hydrates are ice-like, crystalline solids, consisting of guest molecules trapped inside cavities in a framework of hydrogen bonded water molecules [2]. Today, the oil-and gas industry is moving towards increasing water depths and further north, where the temperature and pressure conditions are well within the range for hydrate formation. Presently, most operators are dealing with the hydrate problem using conservative and expensive strategies, assuming that plugging will always occur if the conditions for hydrate formation are present. A new hydrate paradigm is evolving from avoidance of hydrates by inhibition toward risk management which are based on kinetics [3]. Today's knowledge of the physics of hydrate formation and growth is not good enough.

This thesis is a part of the HYADES project which looks at the behavior of hydrate particles in pipelines using experiments in a dedicated HYADES rig and computational simulations, with the main goal of determining the mechanisms leading to hydrate plug formation and possible ways of mitigating this. The objective of this thesis was to set up a Eulerian-Eulerian model using the commercial CFD software ANSYS CFX to study the physics of the formation of a hydrate bed in a horizontal pipe and compare it to experimental results as well as to similar simulations using a different CFD software.

Computational Fluid Dynamics (CFD) is a computer-based tool for simulating the behavior of systems involving fluid flow, heat transfer, and other related physical processes. It works by solving the Navier-Stokes equations over the region of interest, with specified conditions on the boundary of that region.

Computers have been used to solve fluid flow problems for many years. In

the early beginning the CFD codes needed powerful computers and it took large amounts of time to set up the simulations. Consequently, CFD was a tool used almost exclusively in research. Recent advances in computing power, together with powerful graphics have made the process of creating a CFD model and analyzing results much less labor intensive, reducing time and cost. Advanced solvers contain algorithms which enable robust solutions of the flow field in a reasonable time. As a result of these factors, computational fluid dynamics is now an established tool both in research and industry design.

Presently, there have been performed little work neither empirical nor modelling to predict hydrate deposition in a pipeline. This is probably partly due to the difficulties in observing the process in a high-pressure experimental setup. Being able to use CFD to predict if and where hydrates will deposit is of essential importance for e.g the oil and gas industry to be able to convert from using traditional inhibitors to risk managing. To ensure the predictive capabilities of the numerical models it is very important that the CFD-models are validated against experimental results to ensure their performance.

The CFD model for hydrate deposition in a turbulent flow of a slurry containing low-pressure hydrate was build. The model was two-way coupled, i.e both phases interact with each other. Simulations using particle collision models for kinetic theory of granular flows and Gidaspows solids pressure model were performed. The bed thickness predicted by the model was found in qualitatively agreement with the data obtained from experiment [4] and numerical simulations using a different software [1]. Model sensitivities were performed to investigate the effect of the suspension viscosity and the mean particle diameter of the hydrate.

Chapter 2 gives an introduction to hydrates. The chapter contains information on hydrate structure, formation mechanism, plugs, inhibitors and the physical mechanisms which are not fully understood today. Chapter 3 contains useful theory to aid readers which are not familiar with basic flow and computational fluid dynamics theory. Chapter 4 contains a literature review on previous work in the area of solid-liquid flow. Chapter 5 describes the methodology used in this work. Chapter 6 gives the results obtained from this thesis and the results are discussed. Chapter 7 summarize the work and concludes.

Chapter 2

Hydrates

This chapter gives an introduction to hydrates. The chapter contains information on hydrate structure, formation mechanism, plugs, inhibitors and the physical mechanisms which are not fully understood today.

Gas hydrates are crystalline solids composed of water and gas [2]. The gas molecules (guests) are trapped in water cavities (hosts) that are composed of hydrogen-bonded water molecules. The most common gas molecules are methane, ethane, propane and carbon dioxide. The guest molecules have to be small enough to enter these cavities. Larger hydrocarbon molecules than n-butane cannot fit these cages [5]. The structure has the appearance of of ice, but the hydrocarbon molecules inside can make it flammable. Despite of decades of research the mechanism of formation and growth of these structures are not yet fully understood.

2.1 Structure

One of the world's best known example of a chemical phase transition occurs when water at atmospheric pressure is cooled to a temperature of 0°C and turns into ice. At that point, the energy in the system is no longer sufficient to keep the water molecules from bonding together. In this phase transition the water molecules (H_2O) are arranged in a crystal structure with planes of hexagonal rings [6]. The hexagonal rings are held together by the dipole-dipole hydrogen bonds between the electro positive hydrogen atoms and the electro negative oxygen atoms. The van der Waals force is present, but is insignificant compared to the hydrogen bond.

Unlike ice, which only needs water to form crystal structure, hydrates also need guest molecules of a proper size. When the pressure is suitably high, water molecules can make complex crystal structures with planes of hexagonal

rings at temperatures well above the normal freezing point. These structures are quite different from ice structures and are characterized by regular networks of large, open cavities and are inherently unstable. As cooling continues, the normally compact and stable ice structure will ultimately form, unless some outside guest molecule of appropriate size enters the structure without bonding. When a sufficient number of the cavities are occupied, a stable structure is formed. Each cavity can normally only contain one guest molecule unless the pressure is very high [2]. The chemical nature, size and shape of the guest molecules determine which type of hydrate is formed. The hydrate structure, where the guest molecules fill the cavities better, is more stable. The hydrate formation temperature will increase when the hydrate structures get more stable. It is known that hydrates of hydrogen sulphide can exist at temperatures as high as 30°C if the pressure is right [5].

All common gas hydrates belong to three different crystal structures, cubic structure I, cubic structure II or hexagonal structure H [2]. There are some other and more complex structures of gas hydrates, but they are not so common and of less importance [2]. Structure I forms with small guest molecules such as methane, ethane, hydrogen sulfide or carbon dioxide. These guest molecules have a diameter between 4.2 and 6 Å. Nitrogen and small molecules including hydrogen form structure II as single guests. Von Stackelberg [7] discovered that larger guest molecules such as propane or iso-butane will form structure II. These guest molecules have a diameter between 6 - 7 Å and therefore does not fit in the small cavities of structure I. Even larger molecules such as iso-pentane or neohexane can form structure H when accompanied by smaller molecules such as methane, hydrogen sulfide or nitrogen.

Structure I, structure II and structure H hydrates have defined unit cells. The unit cell of type I consist of 46 water molecules, forming two types of cages; small and large [8].There are six large and two small cages in a structure 1 hydrate. The unit cell of type II consists of 136 water molecules, forming eight large and 16 small cages. The unit cell of type H consist of 34 water molecules, forming three types of cages; two small of different type and one large. Information of the cavity type, hydrate structure and which guest molecules that form the different hydrate structures are showed in Figure 2.1. All three common hydrate structures consist of about 85% water, thus many of the hydrate mechanical properties resemble those of ice [2]. Exceptions are. however, thermal expansivity and thermal conductivity which are different from those of ice.

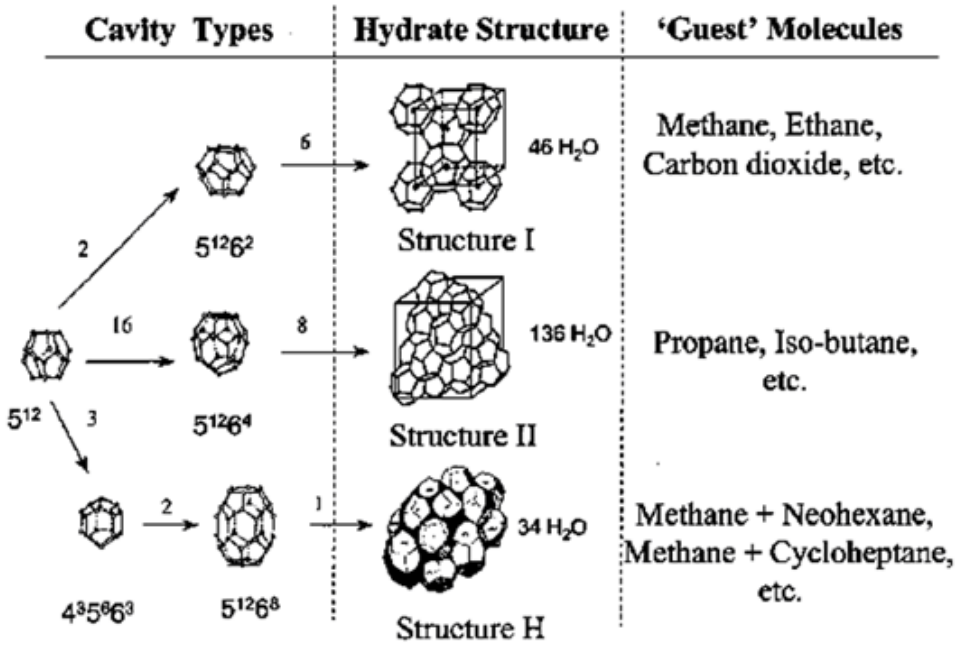

Figure 2.1: *Figure modified from Sloan [2]. Three common hydrate unit crystal structures. Nomenclature: $5^{12}6^4$ indicates a water cage composed of 12 pentagonal and four hexagonal faces. The numbers of cage types are indicated along the arrows. One example is the Structure I unit crystal that is composed of two 5^{12} cages, six $5^{12}6^2$ cages, and 46 water molecules*

2.2 Hydrate formation and growth

The kinetics of hydrate formation and dissociation are considered one of the most intriguing and challenging questions concerning hydrates. Knowledge of hydrate nucleation is of vital importance for e.g the oil and gas industry to be able to predict what conditions hydrates will form under and if hydrate plugs are likely to occur. Despite the fact that a large amount of data are available through many experiments, it has been hard to find any correlation that gives information on when hydrate growth initiates. In general, the formation of hydrate crystals can take place when the mixture of water and guest (gas) molecules are within the pressure and temperature region for hydrate formation. Temperatures are typically < 27°C and pressure typically > 6 bar [3]. The hydrate crystals can grow into large clusters of hydrates.

A phase diagram for natural gas is presented in Figure 2.2. The diagram shows that hydrates can be formed in the region to the left of the line in the

figure. In the region to the right of the line, no hydrates will form. Different gases give different phase diagrams.

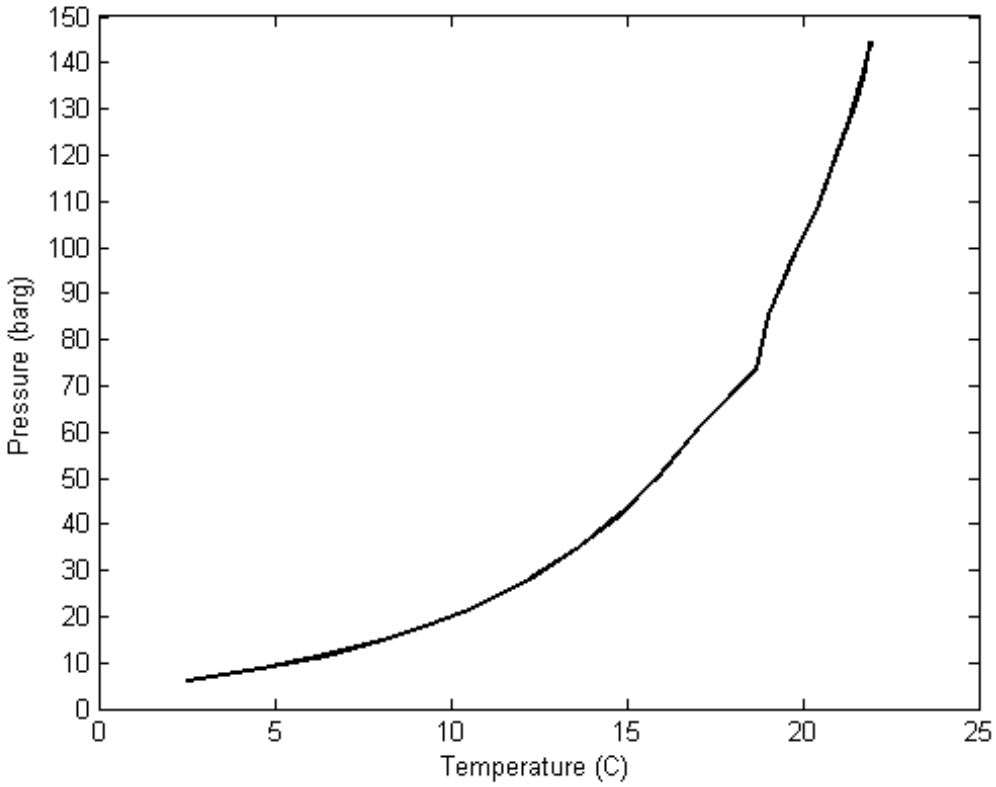

Figure 2.2: *A schematic overview of the behavior of a gas hydrate in a natural gas stream. The gas composition is taken from the gas outlet stream on a 1st stage separator. The phase diagram is calculated by means of the software HYSYS from Aspentech.*

The growth process can be divided into four stages [2]. The growth stages are nucleation, induction time, massive growth and slow growth. These stages are illustrated in Figure 2.3.

The nucleation process is the start of the phase transition where small hydrate crystals try to achieve critical size. When critical size is achieved the crystals continue to grow monotonically if not exposed to competition for mass. This is a random micro scale process, and can not be detected macroscopically.

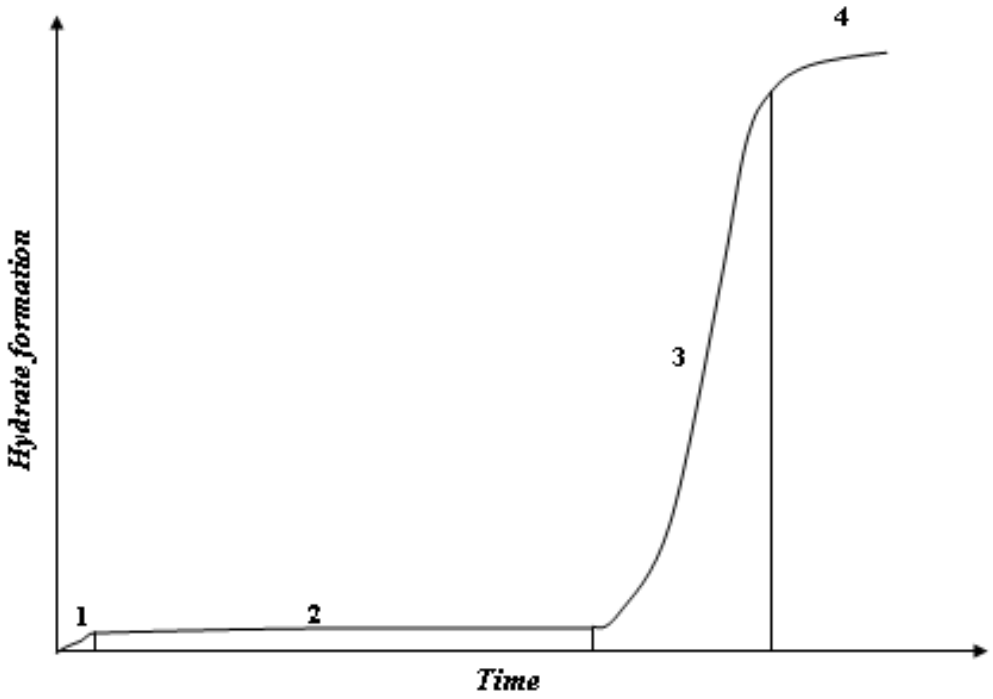

Figure 2.3: *The different stages of hydrate growth. As the induction time comes to an end and hydrate growth has initiated the gas consumption follows an exponential pattern with high initial consumption. Note that this figure only illustrates the stages and that the length and magnitude of each stage will vary.*

Several different hypotheses have been presented on nucleation, whereas three different theories mainly are considered in today's literature [2]. The only way to verify either one of these theories is through experimental work, but due to its stochastic and microscopic nature this is very challenging.

One nucleation hypothesis called "Nucleation at the interface hypothesis" by both Long [9] and Kvamme [10] suggests that the nucleation process consists of four steps [10]:

1. Gas molecules are transported to the interface between water and gas
2. Gas adsorbs on the aqueous surface
3. The gas migrates to a suitable location for adsorption through surface diffusion. At this location the water molecules will first form partial, and then complete cages around the adsorbed molecules

4. Labile clusters will start agglomerate and grow on the vapor side of the surface until a critical size has been reached

The hydrate growth on the gas side of the interface has been estimated to be two magnitudes higher than on the water side [11], and thus the gas side of the interface will dominate the hydrate growth.

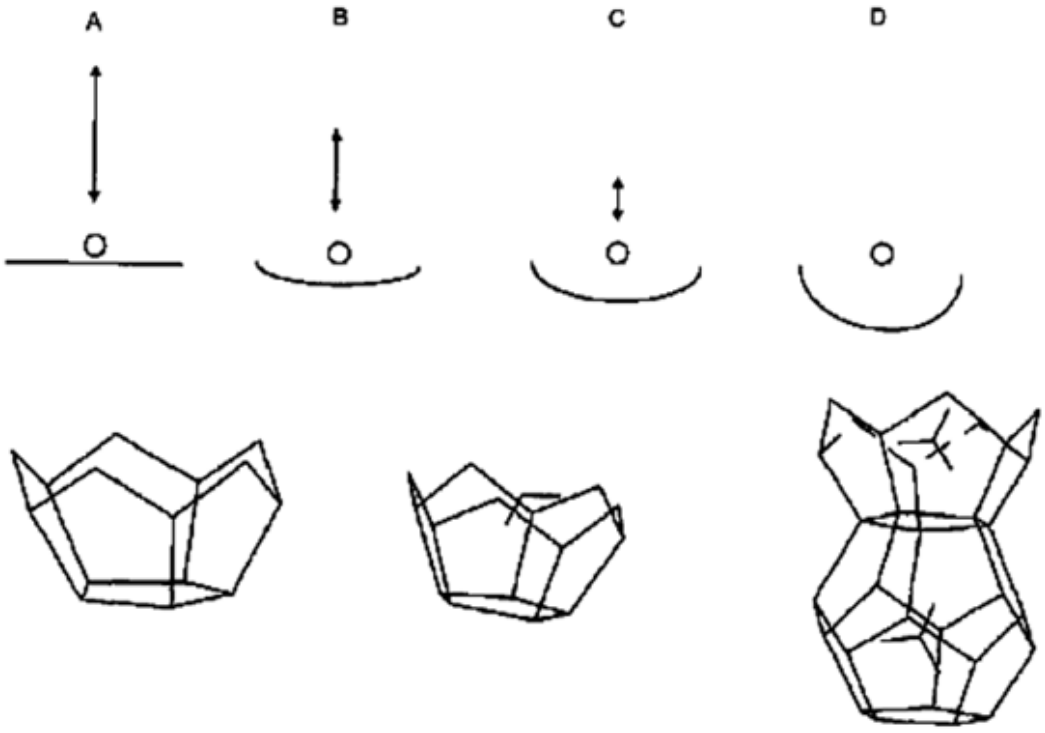

Figure 2.4: *Nucleation at the interface hypothesis. Modified from [12]. A: gas molecule is transported to the gas/water interface. B: The gas molecule migrates to a suitable adsorption location. C: The gas molecule will be encaged in first partial then complete cages. D: Labile clusters agglomerate and start growing on the vapor side.*

The two other common hypotheses on nucleation are the "Labile cluster nucleation hypothesis" [13] and the "Local structuring nucleation hypothesis" [14, 15, 16].

The induction time is the time taken for hydrates to be detected macroscopically to the onset of massive growth. During the induction period, the temperature and pressure conditions are within the hydrate stable region. Experiments have showed that the induction time may vary even though the

variables in the system are kept constant [17]. As a result the induction time is therefore considered a stochastic process.

After the critical size has been reached the massive growth stage is initiated. A very rapid hydrate growth occurs during the massive growth stage. During the growth period, gas is concentrated in the hydrate cages. The hydrated gas molecules are more densely packed than those in vapor. The hydrate growth will then decrease as the water is consumed by hydrate formation.

The hydrate growth process also produces heat. If the surrounding system cannot transport the heat away, the temperature will increase and the growth stop when the temperature exceeds the hydrate formation temperature.

2.3 Hydrate plugs

In the mid- 1930s Hammerschmidt [18] reported that natural gas hydrates were blocking gas transmission lines, frequently at temperatures above the freezing point for ice at atmospheric conditions. This discovery was important in causing a more pragmatic interest in gas hydrates and thereafter led to the regulation of the water content in natural gas pipelines.

Hydrate growth can be a problem in industrial applications and especially in flow assurance. If the temperature, pressure, water fraction and guest gas fraction are right, hydrate formation can occur. The conditions that favors hydrate formation are often found in off-shore pipelines and topside equipment for oil- and gas transportation and processing. Hydrate crystals can agglomerate and plug pipelines and equipment and subsequently cause critical damage to materials, environment and be a potential risk for the exposed personell[19]. Even though new methods to remove hydrate blockages have been discussed in the literature [20, 21], the method implemented so far is through depressurization on both sides of the plug [22]. One problem is that plugs can first dissociate at the pipe wall and thus create a very dangerous projectile. Several incidents where hydrate projectiles have destroyed pipeline bends have occurred. Lysne [23] lists three such incidences where hydrate projectiles erupted from pipelines at elbows and caused the loss of three lives and over US7 million in capital cost.

2.4 Hydrate inhibitors

As mentioned earlier mechanisms behind the formation and growth of hydrates are not yet well established. Accordingly the oil and gas industry uses

the strategy of inhibiting and not preventing the formation and growth of hydrates. Today, there are several possible ways to ensure hydrate inhibition.

1. Remove one of the hydrate components (water or gas)
2. Increase temperature
3. Decrease pressure
4. Inject a component to attract water molecules such as methanol, glycol, thermodynamic inhibitors
5. Inject a component to prevent hydrate agglomeration (anti-agglomerants) or inject a component to prevent sizable crystal growth (kinetic inhibition). These are often called Low dosage hydrate inhibitors

Both water and guest gas are needed to form hydrates. In the industry, the gas is more valuable than water, thus the water is removed. Hydrates consists of 85% water and removing the majority of water will greatly reduce the extent of hydrate formation.

Another way of preventing hydrate formation in pipelines is to change the thermodynamic conditions of the system to conditions where hydrate formation cannot occur. This is done by either increasing the temperature or decreasing the pressure. It is often more convenient to increase the temperature since the pressure is needed to transport the fluid. Increasing the temperature can be done by heating the pipeline (heat trace) or heating the fluid. Offshore pipelines can be very long, and thus heating of the liquid is not possible and heating the pipe will be very expensive. Therefore, the industry injects different chemicals as listed above to prevent hydrate formation or the growth of hydrate particles. These are called inhibitors. The most common ones are described in the next sub chapters.

2.4.1 Thermodynamic inhibitors

To avoid hydrate plugging the oil companies undertake hydrate prevention strategies. Traditionally these strategies are conservative and expensive, assuming that plugging will always occur. In practical applications this strategy means that the transport conditions for hydrocarbons are never allowed to reach the hydrate stable area of the pressure - temperature phase diagram. A common tool for manipulating the phase diagram is thermodynamic inhibitors. Methanol and monoethylene glycols [2] are common thermodynamic inhibitors. As shown in Figure 2.5 the addition of methanol shifts the phase boundary to the left, towards higher pressures and temperatures. This prevention strategy is expensive, because large amounts are required (10-50%

of the water phase [24]). In addition the alcohols must be recovered from the process which is very energy consuming. Hence, if the field is small or the transport length is too long, then the hydrate strategy may be a project stopper. Figure 2.5 shows how injected methanol will shift the hydrate formation region towards higher pressures and lower temperatures.

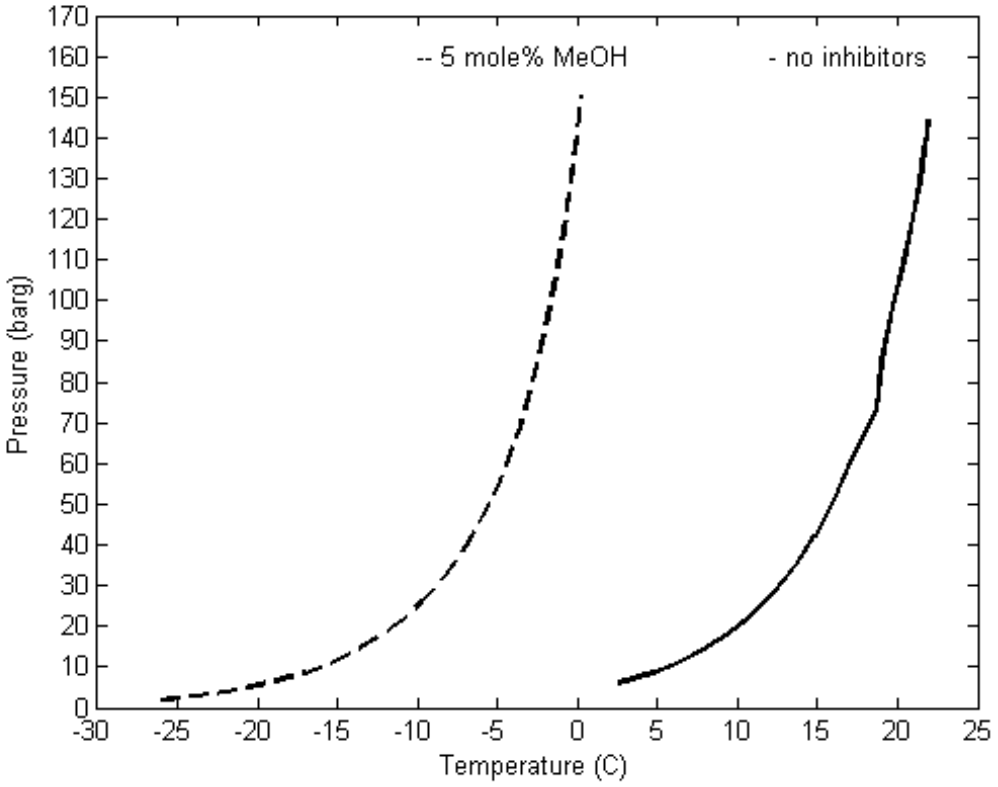

Figure 2.5: *Shift of hydrate equilibrium line towards lower temperatures and higher pressures by addition of 5 vol% methanol (stipple line) compared to a system with no inhibition (black line). The hydrate former is a natural gas taken from the gas outlet on a 1st stage separator from a offshore field. The phase diagrams are calculated by means of the software HYSYS from Aspentech.*

2.4.2 Low dosage hydrate inhibitors

The cost considerations associated with thermodynamic inhibitors have motivated the search for alternative hydrate strategies. The development of

popularly called low dosage hydrate inhibitors, LDHIs, as replacement for alcohols has been a subject of research for decades. A comprehensive review of the literature within this research field is given by Kelland [25]. There exist two main types of LDHIs; anti-agglomerants, AAs, and kinetic inhibitors, KIs.

The anti-agglomerate method which was first introduced in 1987 [2] prevents agglomeration but not formation of hydrates. The method is based on surfactants that provide relatively stable water in-oil emulsions. AA surfactants are thought to work by containing polar head groups that can interact with the lattice of hydrate water molecules, and a hydrophobic tail group that attracts the hydrocarbon phase [19, 26]. Such a mechanism influences the hydrate stability, rendering the hydrate surface oil wet. Oil-wet particles tend to stabilize water-oil emulsions [27, 28]. The AA surfactants are believed to stabilize the water phase as small droplets dispersed in the hydrocarbon phase as a water-oil emulsion, and the hydrates form within these small droplets [2], thus preventing them to stick together and forming plugs. The hydrate suspensions can then easily be transported as slurries in the pipeline. A liquid hydrocarbon phase is required to use anti-agglomerates.

The second group of the LDHIs is the kinetic inhibitors that work by delaying the initial hydrate nucleation [2], i.e. increasing the induction time of hydrate formation. The inhibitors are adsorbed on the hydrate crystal surface to block further growth. This delay in hydrate growth means that one may operate within the hydrate stable area of the phase diagram for a given amount of time without the appearance of hydrates. Kinetic inhibitors are typically water-soluble polymeric compounds [29, 30, 31].

One advantage of using kinetic inhibitors and anti-agglomerants compared to using alcohols, is that a smaller amount have to be added since they are more effective. 1 wt% of AA surfactants is equivalent to 25 wt% methanol. One disadvantage is that the way LDHIs work at a molecular level is not yet fully documented, and the inhibitors are toxic. The main concern is their low biodegradability. The work of developing new and more environmentally friendly LDHIs is currently ongoing [24, 31, 32].

2.4.3 Natural inhibitors

In some cases where crude oil is present in multiphase systems, plugging is never observed even though the system may be located within the stable P-T area of hydrate formation. The natural ability of some crude oils to inhibit hydrate agglomeration has been reported by several authors [27, 33, 34, 35, 36, 37]. This phenomenon is caused by the crude oil composition and the

presence of indigenous hydrate mitigation components. The hydrate mitigation components are believed to be natural anti-agglomerate surfactants with affinity for the hydrate surface, adsorbing to the hydrate surface by hydrogen bonding interactions. As commercial anti-agglomerates the hydrate surface becomes oil-wet. The generation of oil-wet hydrates correlates with the low hydrate plugging tendency, as a result in surface energy of petroleum hydrates [27, 38]. It has been reported that the effectiveness of the natural anti-agglomerants is strongly dependent of the salinity and pH [39].

2.5 Naturally occurring gas hydrates

Preventing hydrate formation in pipelines is not the only motivation to do research on natural gas hydrates. Gas hydrates also occur naturally in many environments, for instance on the ocean floor and in the permafrost [2] and they are a potential energy source. Each volume of hydrate can contain up to 184 volumes of gas at standard temperature and pressure, and thus have very high energy density. The amount of natural gas hydrates have been estimated by several authors, and the amount vary over a wide range [2]. Some authors estimated the amount of carbon in natural gas hydrates to approximately 2.0 x 10^{16} m^3 [40, 41] which can be found both off-shore and on-shore. If correct, this amount would be twice as large as the carbon present in all known fossil fuels [40]. The potential of natural gas hydrates as a future energy resource is discussed in [42]. The author, Beauchamp, stresses that the huge estimates of hydrated gas is not a guarantee for hydrates providing energy supply assurance for the future. The hydrate reservoirs are very uncertain, because they are very dispersed and the solid form makes them difficult to recover [2].

Chapter 3

Basic Theory

This chapter contains useful theory to aid readers which are not familiar with multiphase fluid flow and basic computational fluid dynamic theory. Experienced readers can skip this chapter and still understand the rest of this thesis.

The definition of a fluid is a substance which flows under an applied shear stress regardless of the size of the stress. All liquids and gases are fluids. The flow pattern depends on several quantities. Multiphase flow is any fluid flow which consists of more than two phases (liquid, solid and gas) or one phase consisting of more than one component, as for instance mixture of oil and water. Multiphase flows can be subdivided into four categories; gas-liquid, gas-solid, liquid-solid and three-phase flow. The category treated in this thesis is the liquid-solid flow.

Liquid-solid flow consist of flows in which solid particles are carried by the liquid and are referred to as slurry flows [43]. Slurry flow is considered as a flow regime where the solid particles are suspended in the continuous phase. Slurry flows cover a wide spectrum of applications from the transport of coals and ores to the flow of mud. These flows can also be classified as dispersed phase flows and are the focus of considerable interest in the engineering research.

3.1 Flow types

A fluid can flow through a pipe as a laminar flow or a turbulent flow. In a laminar flow there is no lateral mixing, thus all fluid elements keep their position relative to the cross-section of the pipe. In a laminar flow the velocity, pressure and other flow properties at each point in the fluid stay constant [44]. Laminar flow is observed only where the flow conduit is relatively small, the fluid velocity is low and the viscosity is relatively high.

At higher velocities turbulence appears and vortices form which leads to lateral mixing. Between laminar and turbulent flow the fluid passes through a transitional region with turbulence in the center of the region and laminar near the boundaries [45]. Turbulent flow is highly disordered and the fluid elements move randomly in three dimensions. Figure 3.1 shows the velocity profile of laminar and turbulent flow in a circular pipe. The velocity profile has a parabolic shape for laminar flow.

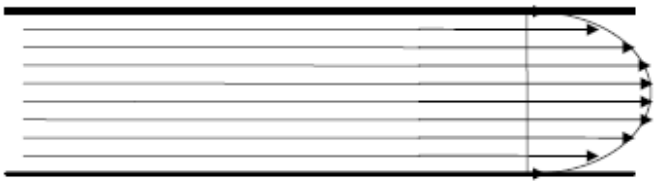

(a) Laminar flow

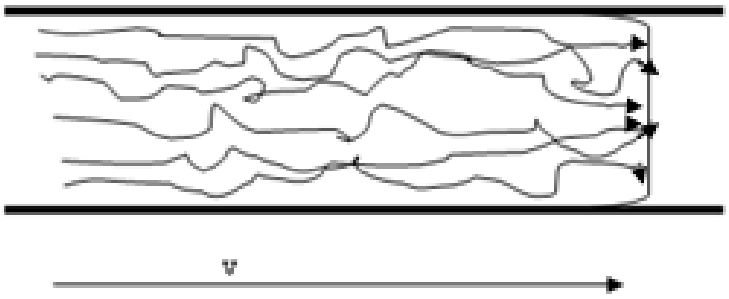

(b) Turbulent flow

Figure 3.1: *Velocity profile of a laminar and a turbulent flow in a pipe.*

Osborne Reynolds was the first to demonstrate the conditions where laminar flow transform to turbulent flow [46]. He found that the critical velocity where laminar flow changes to turbulent flow depends on four quantities; the diameter of the tube, viscosity, density and average linear velocity of the fluid. These four quantities were combined into the dimensionless group called the Reynolds number.

$$Re = \frac{\rho \bar{v} D}{\mu} \tag{3.1}$$

where D is the diameter of the tube, $\bar{v}$ is the average velocity of the fluid, ρ is the density of the fluid and μ is the viscosity of the fluid. The Reynolds number can be used as a guide to if the fluid is laminar, turbulent or in the transitional region. An approximate guide is given by McCabe et al. [44]. Reynolds numbers below 2100 is laminar. Normally the flow in a pipe is turbulent at Reynolds numbers above 4000. Reynolds numbers between 2100 and 4000 is said to be in the transitional region.

3.2 Shear rate and shear stress

Laminar flow can be illustrated as thin layers sliding past eachother. There are no cross-currents or eddies. Two nearby layers will not have the same velocity, thus there is a velocity gradient between them. This velocity gradient is called the shear rate and is defined as

$$\frac{du}{dy} = \lim_{y \to 0} \frac{\Delta u}{\Delta y} \tag{3.2}$$

where u is the local velocity and y is the distance from the wall.

Fluids resist shear, thus a shear force exists wherever there is a shear rate. This shear arise from adjacent layers trying to affect the other. The faster layer tries to increase the velocity of the slower plate, and opposite, the slower layer tries to decrease the velocity of the faster layer. There is therefore a force F_s acting on the slower layer and a equally large force with opposite direction on the faster layer. The force per unit area between the shearing layers are called the shear stress. The shear stress is denoted τ and defined as

$$\tau = \frac{F_s}{A_s} \tag{3.3}$$

where A_s is the area of the plane between the layers. Shear forces are generated in both laminar and turbulent flow.

3.3 Properties of dispersed phase flows

Dispersed phase flow is flow where one phase is not materially connected. The density at one point of a continuum is defined as

$$\rho = \lim_{\delta V \to 0} \frac{\delta M}{\delta V} \tag{3.4}$$

where δM is the mass associated with the volume δV. Since real material are not strictly speaking a continuum, the limiting volume δV^0 cannot be zero.

The volume must be large enough to contain at least 10^4 molecules which correspond to a cube where the sides are minimum 10^{-7} m [43]. This cube size is calculated based on the assumption that one mole of gas at standard conditions contains 10^{23} molecules and occupies a volume of approximately 22 liters.

The volume fraction of the dispersed phase is defined as

$$\phi_d = \lim_{\delta V \to \delta V^o} \frac{\delta V_d}{\delta V} \tag{3.5}$$

where δV_d is the volume of the dispersed phase in the volume. Equivalently, the volume fraction of the continuous phase is

$$\phi_c = \lim_{\delta V \to \delta V^o} \frac{\delta V_c}{\delta V} \tag{3.6}$$

where δV_c is the volume of the continuous phase in the volume. The sum of the volume fractions must be unity.

$$\phi_d + \phi_c = 1 \tag{3.7}$$

The bulk density of the dispersed phase is the mass of the dispersed phase per unit volume of mixture and defined as

$$\bar{\rho}_d = \lim_{\delta V \to \delta V^o} \frac{\delta M_d}{\delta V} \tag{3.8}$$

where δM_d is the mass of the dispersed phase.

The mass of the dispersed phase can be written as

$$\delta M_d = \rho_d \delta V_d \tag{3.9}$$

where ρ_d is the density of the dispersed phase material. Equation 3.9 can be inserted into equation 3.8 which gives

$$\bar{\rho} = \lim_{\delta V \to \delta V^o} \frac{\rho_d \delta V_d}{\delta V} = \rho_d \lim_{\delta V \to \delta V^o} \frac{\delta V_d}{\delta V} = \rho_d \phi_d \tag{3.10}$$

The same can be done for the continuous phase

$$\bar{\rho}_c = \rho_c \phi_c \tag{3.11}$$

The sum of the bulk densities is the mixture density

$$\bar{\rho}_d + \bar{\rho}_c = \rho_m \tag{3.12}$$

An alternate expression for the mixture density can be obtained by inserting equation 3.10 and equation 3.11 which gives

$$\rho_m = \phi_c \rho_c + \phi_d \rho_d \tag{3.13}$$

3.4 Dilute versus dense flow

A dilute dispersed flow is one where the particle motion is controlled by the fluid force (drag and lift). A dense flow is one in which the particle motion is controlled by collisions. A flow can be considered dilute if

$$\frac{\tau_V}{\tau_C} < 1 \tag{3.14}$$

where τ_V is the relaxation time of the particle (the time for the system to reach equilibrium after a disturbance). τ_C is the average time between particle-particle collisions because the particles have sufficient time to respond to the local fluid dynamic forces before the next collision. If

$$\frac{\tau_V}{\tau_C} > 1 \tag{3.15}$$

then the particles have no time to respond to the fluid dynamic forces before the next collision and the flow is dense.

3.5 Stokes number

The Stokes number is a very important parameter in fluid-particle flows. It is defined as the ratio of the stopping distance of a particle to a characteristic dimension of the obstacle.

$$St_V = \frac{\tau_V v}{D_T} \tag{3.16}$$

where v is the fluid flow velocity far away from the obstacle and D_T the characteristic dimension of the obstacle.

If $St_V << 1$, the response time of the particles is much less than the characteristic time associated with the flow field. The particles will have time to respond to changes in velocity. Thus the particle velocity will be equal to the flow velocity. If the $St_V >> 1$, the particles are not affected by the continuous fluid. Their response time is longer than the time the fluid has to act on it. Thus, the particle will pass through the flow without much deflection on its initial trajectory.

3.6 Momentum coupling

Coupling is an important concept in the analysis of multiphase flows. If the flow of one phase affects the other while there is no reverse effect, the flow is said to be one-way coupled. On the other hand, if there is a mutual effect between the flows of both phases, then the flow is two-way coupled. Coupling can take place through mass, momentum and energy transfer between phases. Mass coupling is the addition of mass through evaporation or the removal of mass from the carrier stream by condensation. Energy coupling occurs through heat transfer between phases. Momentum coupling is the result of the drag force on the dispersed and continuous phases.

A momentum coupling parameter can be defined as

$$\Pi_{mom} = \frac{D_d}{Mom_c} \tag{3.17}$$

where D_d is the drag force due to the particles in the volume and Mom_c is the momentum flux through the volume. The drag associated with particles in volume with side L is

$$D_d = nL^3 3\pi\mu_c D\,(u - v) \tag{3.18}$$

based on Stokes drag. The momentum flux of the continuous phase is given by

$$Mom_c = \bar{\rho}_c u^2 L^2 \tag{3.19}$$

The momentum coupling parameter can be expressed as

$$\Pi_{mom} = \frac{nmL}{\bar{\rho}_c u \tau_V}\left(1 - \frac{v}{u}\right) \tag{3.20}$$

where m is the mass of an individual element of the dispersed phase. The product nm is the bulk phase density of the dispersed phase. Thus, the importance of momentum coupling can be assessed by the parameter

$$\Pi_{mom} \sim C\frac{L}{u\tau_V}\left(1 - \frac{v}{u}\right) \tag{3.21}$$

The ratio $\tau_V u/L$ is the ratio of the time associated with momentum transfer to a time characteristic of the flow or the Stokes number for momentum transfer.

$$St_{mom} = \frac{\tau_V u}{L} \tag{3.22}$$

The momentum coupling parameter can be expressed as

$$\Pi_{mom} = \frac{C}{St_{mom}} \left(1 - \frac{v}{u}\right) \tag{3.23}$$

Using the fact that the velocity ratio can be expressed as

$$\alpha = \frac{u_d}{u_c} \sim \frac{1}{1 + St_V} \tag{3.24}$$

the momentum coupling parameter becomes

$$\Pi_{mom} = \frac{C}{1 + St_{mom}} \tag{3.25}$$

which shows the correct limit as the Stokes number approaches zero. Momentum coupling effects become less important for small concentrations and large Stokes numbers.

3.7 Particle size distribution

Particle size affect the flow of a dispersed two-phase mixture, thus it is important to know the particle size distribution. A good way to measure the particle size is to use the diameter. The mean diameter of the particles and the standard deviation can be used to determine how the particle sizes are distributed. The mean diameter can be found from

$$\overline{D}_n = \sum_{i=1}^{N} D_i f_n \left(D_i\right) \tag{3.26}$$

The variance is a measure of the spread of the distribution and is defined as

$$\sigma_n^2 = \sum_{i=1}^{N} D_i^2 f_n \left(D_i\right) - \overline{D}_n^2 \tag{3.27}$$

The standard deviation is the square root of the variance

$$\sigma_n = \sqrt{\sigma_n^2} \tag{3.28}$$

If the standard deviation is less than ten percent of the mean particle size, the particles have a monodispersed distribution [43]. If the standard deviation is greater than ten percent, the particles have a polydispersed distribution.

3.8 Boundary layer

A boundary layer is defined as that part of a moving fluid in which the fluid motion is influenced by the presence of a solid boundary [44]. The fluid velocity at the solid-fluid interface is zero, and the velocities close to the solid surface are small. Flow in this part of the boundary layer very near the surface is therefore essentially laminar. Further away from the surface the fluid velocities may be fairly large and flow in this part of the boundary layer may become turbulent. Between the zone of fully developed turbulence and the region of laminar is a transition zone called the buffer layer. Thus a turbulent boundary layer is considered to consist of three zones: the viscous sublayer, the buffer layer and the turbulent zone. The development of turbulent boundary layer on a flat plate is shown in Figure 3.2.

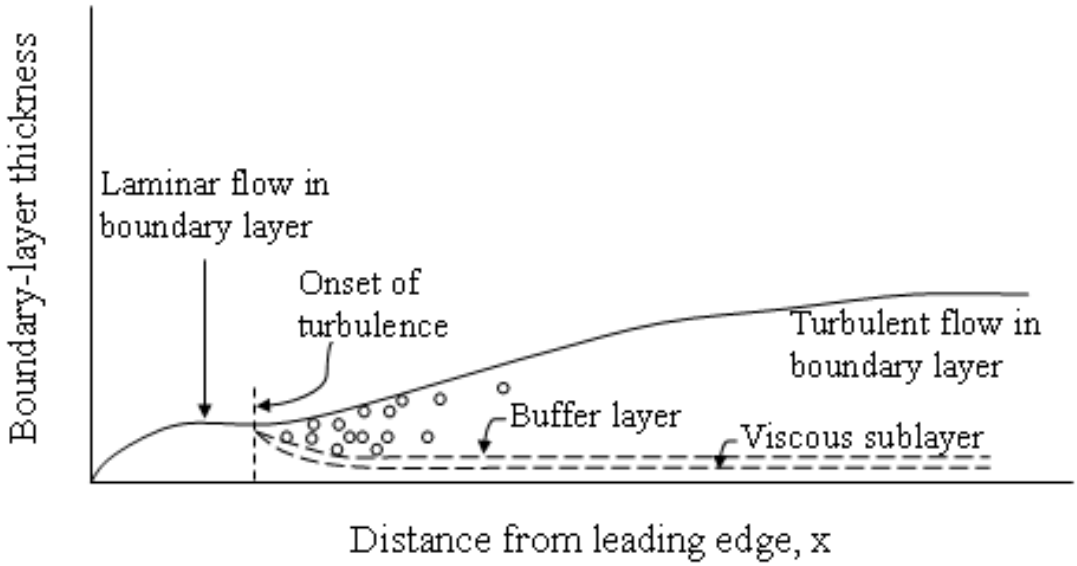

Figure 3.2: *Development of turbulent boundary layer on a flat plate (The vertical scale is greatly exaggerated).*

As shown in Figure 3.2 the onset of turbulence is characterized by a sudden rapid increase in the thickness of the boundary layer.

3.9 Two-fluid model

Many approaches exists for modelling the motion of two-phase mixtures (e.g. solid - liquid), where one phase is dispersed in the other. They can be divided into Eulerian - Eulerian and Eulerian - Langrangian approaches. The Eulerian - Eulerian two fluid model is used in this thesis.

In the Eulerian - Langrangian approach the dispersed phase is treated in terms of individual particles for which equations of motion are solved. On the other hand the Eulerian - Eulerian [47] two-fluid model assumes that the phases present in the system behave like a continuum (the dispersed phase is treated as a second fluid that moves in space together with the liquid phase). This method can be employed either for mixtures of immiscible fluids, such as bubbly flows, or for dispersed flows involving the presence of small-scale entities such as particles or droplets. From the mathematical modelling point of view both fluids are described by similar equations of conservation and this is an advantage of the approach.

3.10 Governing equations

Computational Fluid Dynamics (CFD) is based on the fundamental governing equations of fluid dynamics; the continuity, momentum and energy equation. These equations are mathematical statements of three fundamentally physical principles which all of fluid dynamics are based on:

1. Mass is conserved
2. Newton's second law
3. Energy is conserved

The equations describing the process of momentum, heat and mass transfer are known as the Navier-Stokes equation named after Claude-Louis Navier and George Gabriel Stokes [48]. These partial differential equations were derived in the early nineteenth century and have no known general analytical solution but can be discretized and solved numerically [48]. The set of equations solved by ANSYS CFX are the unsteady Navier-Stokes equations in their conservation form.

The continuity equation in conservation form can be written as:

$$\frac{\delta \rho}{\delta t} + \nabla \cdot (\rho V) = 0 \tag{3.29}$$

The momentum equation in conservation form can be written as

$$\rho\frac{Du}{Dt} = -\frac{\delta\rho}{\delta x} + \frac{\delta\tau_{xx}}{\delta x} + \frac{\delta\tau_{yx}}{\delta y} + \frac{\delta\tau_{zx}}{\delta z} + \rho f_x \tag{3.30}$$

which is the x component for a viscous flow. y and z components can be written similarly.

The energy equation in the conservation form in terms of total energy $e + (V^2)/2$ is written as:

$$\begin{aligned}
&\frac{\delta}{\delta t}\left[\rho\left(e + \frac{V^2}{2}\right)\right] + \bigtriangledown\cdot\left[\rho\left(e + \frac{V^2}{2}\right)V\right] \\
&= \rho q + \frac{\delta}{\delta x}\left(k\frac{\delta T}{\delta x}\right) + \frac{\delta}{\delta y}\left(k\frac{\delta T}{\delta y}\right) + \frac{\delta}{\delta z}\left(k\frac{\delta T}{\delta z}\right) - \frac{\delta(up)}{\delta x} - \frac{\delta\,(vp)}{\delta y} - \frac{\delta\,(wp)}{\delta z} \\
&\quad + \frac{\delta\,(u\tau_{xx})}{\delta x} + \frac{\delta\,(u\tau_{yx})}{\delta y} + \frac{\delta\,(u\tau_{zx})}{\delta z} + \frac{\delta\,(v\tau_{xy})}{\delta x} + \frac{\delta\,(v\tau_{yy})}{\delta y} + \frac{\delta\,(v\tau_{zy})}{\delta z} \\
&\quad + \frac{\delta\,(w\tau_{xz})}{\delta x} + \frac{\delta\,(w\tau_{yz})}{\delta y} + \frac{\delta\,(w\tau_{zz})}{\delta z} + \rho f\cdot V
\end{aligned} \tag{3.31}$$

Chapter 4

Literature survey

This chapter contains an overview of earlier work on particle deposition and bed formation. Little work has been published in particle deposition in solid-liquid flow. The search for literature has been broadened to include properties of slurry flow, deposition in solid-gas flow and the effect of particle collision on particle deposition.

Multiphase solid-liquid / solid-gas flows are important in a wide range of industry applications, e.g. the oil and gas, and the process industry. It has therefore been of interest to many researchers. Although much emphasize has been done to simulate dense two-phase flow (e.g fluidized beds), less emphazise has been given to the particle deposition and the mechanisms of deposition are not fully understood. The deposition mechanisms is important in the oil and gas industry for them to be able to predict the formation of hydrate or wax plugs.

4.1 Deposition in hydrate slurries

A literature search reveals that several experimental investigations [49, 50, 51] on hydrate slurries have been done for the elucidation of the rheological and frictional behavior of such slurries, although the problem of hydrate deposition was not considered there. This might be related to insufficient insight into the flow morphology caused in part by the difficulties of slurry visualization [52]. Balakin et al. [4] performed experiments in a flow loop using Freon R 11 hydrate. The experiments showed that the hydrate particles created at low volume fractions were observed not to influence the flow significantly, i.e. the pressure drop, mixture density and mass flowrate were insignificantly different from those of pure water. At these low volume fractions a hydrate bed was detected in the horizontal pipe regions at low flowrates. Balakin

et al. [52] built a multiphase CFD-model for hydrate deposition based on the experiment reported by Balakin et al. [4]. The particle diameter was decreased with an increase in the turbulence intensity of the system. The hydrate bed was formed when the gravity force became dominant compared to the combination of buoyancy $F_{A,h}$ and the drag force $M_{a,h}$ because of the increased mean particle size. The thickness of the bed predicted by the model was in good accordance with the experimental results.

4.2 Modelling approach on solid-liquid flow

As mentioned above little work has been done on the deposition of hydrate particles. In a bit broader search within solid-liquid flow more work is found. In the past many researchers have attempted to develop methods for predicting the characteristics of horizontal solid-liquid flows using different approaches. In parallel with the increase in computer power the use of numerical models has turned from simplified analytical models to comprehensive computational models. One popular approach has been to correlate empirical data using phenomenological reasoning [53]. Another approach has been to develop simplified analytical models, such as two and three layer models [54]. A more mechanistic approach is to predict these flows using multidimensional two-fluid computational fluid dynamic (CFD) models which have physically based interfacial closure laws [55].

Detailed measurements in flowing solid-liquid experiments are difficult to perform, since standard intrusive instrumentation may be damaged by particle impact. The primary parameters of interest have been the local volume fractions, mean velocities, turbulence intensities and the Reynolds stress for each phase. These measurements are important to understand the physical mechanisms which control phase distribution processes in solid-liquid flows.

Comprehensive experimental results have been published for small particles (e.g. sand), in which the turbulent eddies of the continuous phase were much larger than the dispersed particles [56, 57].

4.3 Slurry flow

Much work has been done on models for slurry flows. Most engineering models on slurry flows have focused on the ability to predict frictional pressure loss and minimum operating velocity (deposition velocity) for coarse-particle

slurries. Many models of this type exist and have varying degrees of success in predicting the mentioned parameters.

Durand [58] published an experimental work where the basic relationships of the transportation of solids in pipe were studied. Durand classified the flow regimes as a "non-deposit flow regime" or a "regime with deposits". The deposition velocity was used to mark the separation between the two regions and called the "limit deposit velocity". An empirical method to predict hydraulic gradients for the coarse particle slurry flow was developed. Wasp et al. [59] improved the calculations method and applied it to commercial slurry pipeline design. Shook and Daniel [60] used the pseudo homogeneous approach to model slurry flow. The turbulent flow of suspensions of fine solid particles in liquids were analyzed by assuming that the suspensions behave essentially as variable-density single phase fluids. The unique aspect of this technique is that it allows description of the flow using a single set of conservation equations (as for single phase flow).

Oroskar and Turian [61] used a constructive energy approach to calculate the deposition velocity. In their model, they assumed that the kinetic energy of turbulent fluctuations is transferred to discrete particles, which suspends them in the flow. The predicted deposition velocities compared well with experimental data over a wide range of solids volume fractions.

Wilson and Pugh [62] developed a dispersive force model of heterogeneous slurry flow, which extended the applicability of the original Wilson layer model [63] because it accounted for particles suspended by the fluid turbulence as well as those providing contact-load (Coulombic) friction. The model was used to predict particle concentration and velocity profiles that were in good comparison with experimental measurements.

The most commonly used two-layer model is the SRC model developed by Gillies and co-workers [64, 65, 66, 67]. The SRC two-layer model provides predictions of pressure gradient and deposition velocity as a function of particle diameter, pipe diameter, solids volume fraction and mixture velocity.

Doron and Barnea [54] extended the two-layer modelling approach to a three-layer model of slurry flow in horizontal pipelines. Their model considered the existence of a dispersive layer, which is between the suspended layer and a bed. The dispersive layer was considered to have a higher concentration gradient than the suspended layer. The model predictions showed satisfactory agreement with experimental data.

Ekambara et al. [68] developed a comprehensive computational model to describe the hydrodynamics of horizontal slurry flow based on the kinetic theory of granular flow. The model gave in general good agreement between the predicted and the experimental data which was obtained for a wide range of in situ solids volume fractions, particle diameters, mixture velocities and pipe diameters. The CFD model described was capable of predicting particle concentration profiles for fine particle slurries where fluid turbulence is effective at suspending the particles. It also performed satisfactorily when the particles are coarse and concentration profiles are primarily dependent upon the in situ solids volume fraction. In experimental data sets where the near-wall lift force was of sufficient magnitude to cause a reversal in the concentration profile near the pipe invert, the CFD model was not able to reproduce that behavior.

4.4 Gas-solid flow

In the first part of this chapter previous work in modelling and experiments on solid-liquid flow has been discussed. Another field of interest is the work on particle transport and deposition in gas-solid flow. Work on particle transport and deposition in solid-gas flow has been reported in the literature since the process is significant in various fields of engineering and natural science [69, 70, 71, 72, 73].

Because of simultaneous influences from fluid flow convection, particle-boundary hydrodynamic interaction, colloidal interaction, molecular diffusion and external applied body forces, particle deposition onto a surface is an extremely complicated process [69].

Chein et al. [69] found that a particle could be suspended above or deposited on the wall depending on the Hamaker constant (a constant reflecting the surface potentials of the particle and wall), and the thickness of the electrical double layer.

Another work by Yang et al. [73] studied the partical deposition process in solid-gas flow in a conceptual manner. They divided the process into four steps according to the distance between the particle and the surface:

1. When the distance is large, the particle transport is controlled by the fluid convection and external body forces.

2. As the distance becomes comparable to the particle size, additional forces start to act on the particle due to the presence of the wall. These forces, known as particle-wall hydrodynamic interactions, reduce the particle mobility.

3. When the distance becomes within the range of 1 - 100 nm, the van der Walls and the electric double-layer forces start to affect the particle motion. This is due to the interaction between the surface potentials of the particle and the wall. These two interactions form the basis of the well known DLVO theory of colloidal stability [74, 75]. The sum of these two interaction forces plays an important role in determining the particle behavior in the near-wall region. Generally, the magnitude of the colloidal force depends on the Hamaker constant, particle size, ionic strength of the suspension medium, and surface potentials of the two interacting surfaces.

4. At smaller distance than 1 nm the particles are considered to adhere to the wall when the van der Waals force is attractive.

Jassim et al [76] studied the mechanism of particle deposition for methane hydrate in a turbulent gas stream with use of computational fluid mechanics. The particle deposition can be explained by two mechanisms depending on the particle size. The very small particles, roughly with diameters less than one micrometer, deposit as a result of the Brownian effect, i.e the particles exhibit a random motion as a result of their continuous bombardment by the molecules of the surrounding gas [71]. On the other hand the deposition of relatively larger particles is controlled by the gravitational and inertia settling. In the Brownian regime, the collection deposition was high for very small particles and became less as the particles grow. In contrast, in the inertia regime, the collection efficiency increased with the particles size. Another conclusion obtained from the analysis was that the particles velocity profile is similar to the profile of the carrier fluid. However, as the particle size increased the particles moved at slower mean velocities compared with the carrier fluid.

4.5 Modelling of particle collisions

Another technique used for simulating particle deposition in two-phase flows is the Eulerian-Langrangian approach, where the solid phase is modelled as a system of individual points, subject to forces according to their size and

shape [43]. This technique involves the problem of modelling of collisions, both between particles and particles with walls. One of the most popular technique is the hard sphere model [43]. Two hard-sphere collision models are widely in use. The first of Hoomans et al. [77] and the second by Crowe at al. [43]. The drawback of these models is that they do not take into account cohesion between the particle or adhesion of a particle to a wall. As a result particles will bounce off after a collision, even though their initial speed, size, and surface properties indicate that they should not escape the collision but rather result in the formation of an agglomerate. Cohesion and adhesion are essential elements in a wide range of processes i.e the formation of hydrate or wax plugs in pipelines in the oil and gas industries [78].

Much of the research aimed at modelling particle cohesion has been dedicated to the simulation of fluidized bed [79, 80, 81, 82]. Basically cohesive forces can be included in Eulerian-Langrangian simulations in two ways. The first strategy is to include the cohesive force in the particle equation of motion and thus simply include it as an extra force acting on the particle in the numerical scheme. This strategy has mostly been focused to extend the soft-sphere model [83, 84]. The second strategy is to incorporate the cohesive force in an impulse-based collision model. Kosinski et al. [78] used this strategy to develop an extension of the standard hard-sphere particle-wall collisions model to account for particle adhesion. This extended hard-sphere model was compared with the standard one. The main difference was showed at lower initial velocities where the standard hard-sphere model was not able to simulate deposition and the particles bounce off even under conditions where deposition might be expected.

Chapter 5

Methodology

The CFD-model described in this thesis is based on experiments reported in Balakin et al. [4], which were done in a low-pressure flow loop for water-Freon R 11 hydrate slurry. The experiment was carried out using variable hydrate slurry concentrations. The loop, shown in Figure 5.1, consisted of a set of transparent PVC-pipelines, a centrifugal pump, a Coriolis flowmeter and a number of gauge pressure probes for measurements of frictional pressure loss.

It was shown in the experiments that the flow behavior of the hydrate slurry depends on the mean flow velocity as well as the solid volume fraction. The hydrates in the water suspension have the characteristics of a non-Newtonian fluid with positive yield stress values under conditions of low flow. The hydrate particles created at low volume fractions of freon were observed not to influence the flow significantly, i.e. the pressure drop, mixture density and mass flowrate were insignificantly different from those of pure water. At these low volume fractions a hydrate bed was detected in the horizontal pipe regions at low flowrates, together with a dilute solids suspension in the bulk upper part of the pipe. This bed was lifted up into the upper part of the pipe and making the suspension become homogeneous when the mean flow velocity was increased beyond 0.4 m/s.

5.1 Model setup

5.1.1 Geometry

The horizontal section downstream the pump in the experimental rig [4] included a 90 degree bend was generated with ANSYS Designmodeler. The dimensions were taken from the experimental rig. The length of the horizontal pipe section was 450 mm, the radii of the bend 105 mm and the vertical

Figure 5.1: *Photo of the experimental flow loop by Balakin et al. [4]. (1 - Centrifugal pump; 2 - Expansion tank; 3 - Thermocouple; 4,5 - Pressure sensors; 6 - Sampling unit; 7 - Ventilation; 8 - Safety valve; 9 - Flow meter; 10 - Pressure sensor, 11 - Drainage). Adopted by courtesy of Boris Balakin.*

pipe section 200 mm. The diameter of the pipe was 45.2 mm. The CAD-geometry used in this thesis is presented in Figure 5.2.

5.1.2 Grid generation

The partial differential equations that govern fluid flow and heat transfer are not usually possible to solve analytically. Therefore, in order to analyze fluid flow, flow domains are split into smaller subdomains and the discretized governing equations are solved inside each of these portions of the domain. ANSYS CFX uses an element-based finite volume method, which first involves discretization the spatial domain using a grid [85]. The grid is used to construct finite volumes, which are used to conserve relevant quantities such as mass, momentum and energy.

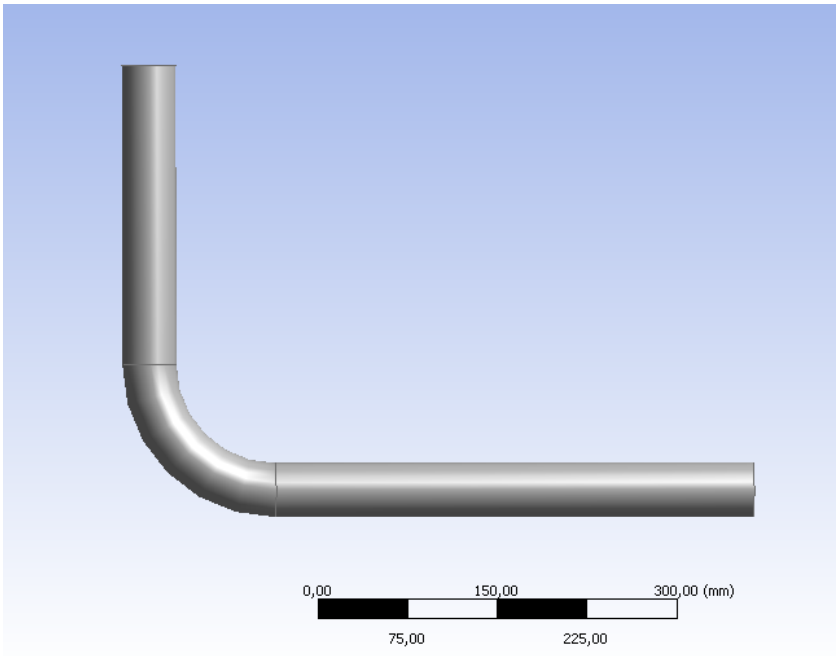

Figure 5.2: *Three-dimensional CAD-model of the flow loop test section.*

The discretization of the three-dimensional domain resulted in total of 70 552 elements. 37 572 tetrahedrons and 32 980 prisms. Five inflated layers (prisms) were put near the wall to encount for the boundary layer effects in the near-wall regions. Pictures of the grid can be seen in Figure 5.3a and 5.3b.

5.1.3 Fluid settings

The CFD model was created defining two fluids. Water was used as the continuous phase with a mass density of 1000 kg/m^3, molar mass of 18.02 g/mole and a viscosity of 0.001 Pa s. The dispersed hydrate phase is modelled as a dispersed solid with a mass density of 1140 kg/m^3 [86] and a molar mass of 137 g/mole. A different set up were used with respect to the dispersed hydrate viscosity. Both constant viscosity and a expression as a function of the hydrate volume fraction were used.

5.1.4 Boundary conditions

At the inlet, velocities and concentrations of both phases were specified. At the outlet, the pressure was specified (atmospheric). At the wall, the no-slip

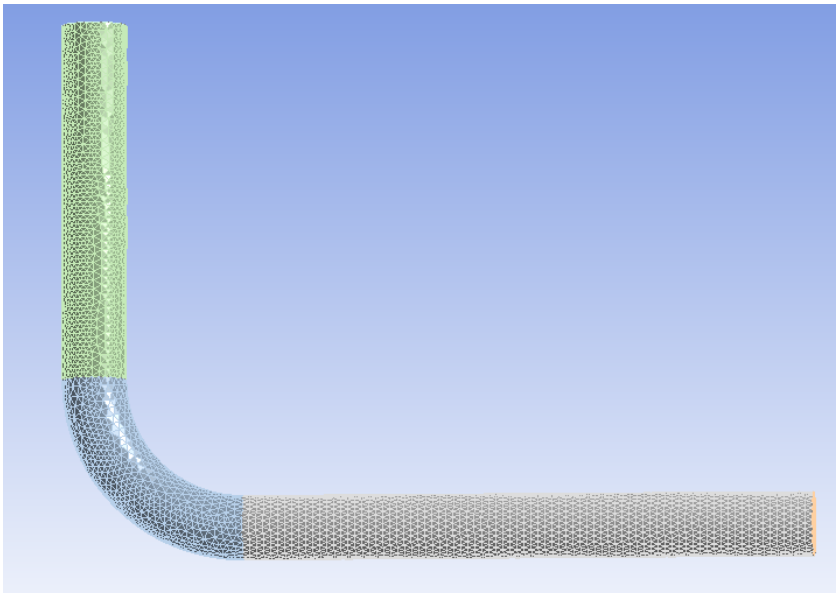

(a) Grid structure on the surface of the pipebend

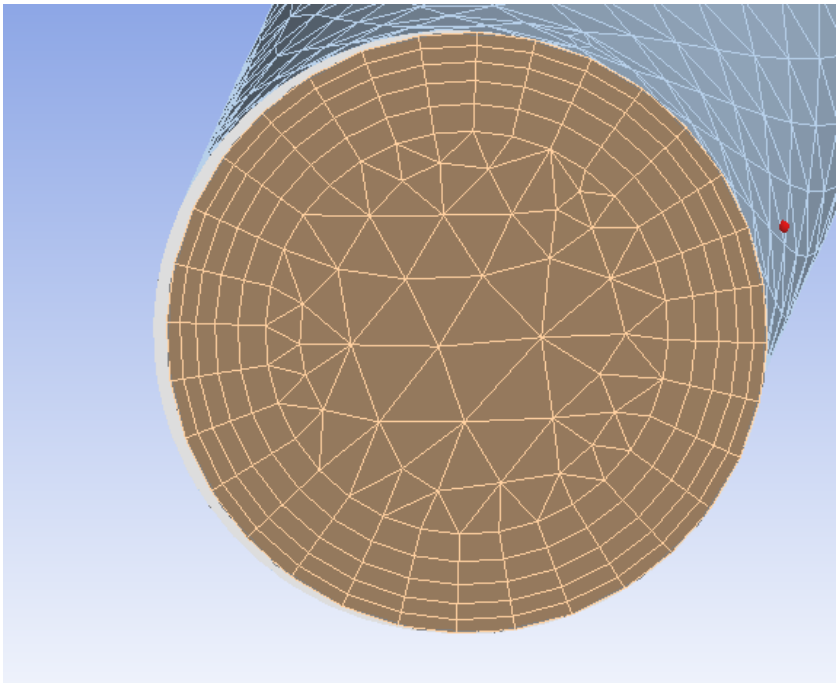

(b) Grid structure of the volume mesh consisting of tetrahedons and prisms.

Figure 5.3: *Three-dimensional CAD-model of the experimental test section discretized with tetrahedrons and prisms. The prismatic layers near the wall is to encount for the boundary layer effects in the near-wall regions.*

conditions were specified for both phases, i.e the velocity at the wall is set to zero.

5.1.5 Multiphase model

Multiphase flow was treated using the Eulerian-Eulerian two-fluid model [87], the flow was considered to be turbulent, isothermal, with no interphase mass transfer.

The inhomogeneous model [85] was chosen, i.e. each fluid possesses its own flow field and the fluids interact via interphase transfer terms. In the inhomogeneous multiphase model, there is one solution field for each phase (velocity field, turbulence field etc.). Transport quantities interact via interphase transfer terms. For example, two phases may have separate velocity and temperature fields, but there will be a tendency for these to come to equilibrium through interphase drag and heat transfer terms. The inhomogeneous model is the opposite to the homogeneous model where both phases are assumed to share the same velocity field, turbulence field etc.

Interfacial transfer of momentum, heat and mass is directly dependent on the contact area between the two phases. This is characterized by the interfacial are per unit volume between phase α and phase β, known as the interfacial area density, $A_{\alpha\beta}$. To model the interfacial transfer the particle model is used, which essentially provide the algebraic prescriptions for the interfacial area density. The particle model assumes that one of the phases is continuous (phase α) and the other is dispersed (phase β). The surface area per unit volume is then calculated by assuming that phase β is present as spherical particles of means diameter d_β. Using this model a simplified expression for the interfacial area density can be written as:

$$A_{\alpha\beta} = \frac{6\phi_\beta}{d_\beta} \tag{5.1}$$

where ϕ_β is the volume fraction of the dispersed phase.

Non-dimensional interphase transfer coefficients may be correlated in terms of the particle Reynolds number and the fluid Prandtl number. These are defined using the particle mean diameter and the continuous phase properties, as follows:

$$Re_{\alpha\beta} = \frac{\rho_\alpha |U_\beta - U_\alpha| d_\beta}{\mu_\alpha} \tag{5.2}$$

$$Pr_{\alpha\beta} = \frac{u_\alpha C_{P\alpha}}{\lambda_\alpha} \tag{5.3}$$

5.1.6 Turbulence model

The $k-\epsilon$ turbulence model was used for the continuous phase. The dispersed phase zero equation was used for the dispersed phase.

The standard $k-\epsilon$ model is a semi-empirical model [88] based on model transport equations for the turbulent kinetic energy, k, and its dissipation rate, ϵ. ϵ is the variable that determines the scale of the turbulence, whereas the first variable, k, determines the energy in the turbulence. In the derivation of the $k-\epsilon$ model, it was assumed that the flow is fully turbulent, and the effects of molecular viscosity are negligible.

The turbulent kinetic energy, k, and its rate of dissipation, ϵ, are obtained from the following transport equations

$$\frac{\delta(\rho k)}{\delta t} + \frac{\delta(\rho U_j k)}{\delta x_j} = P_k - \rho\epsilon + \frac{\delta}{\delta x_j}\left(\Gamma_k \frac{\delta k}{\delta x_j}\right) \tag{5.4}$$

and

$$\frac{\delta(\rho\epsilon)}{\delta t} + \frac{\delta(\rho U_j \epsilon)}{\delta x_j} = C_{\epsilon 1}\frac{\epsilon}{k}P_k - C_{\epsilon 2}\rho\frac{\epsilon^2}{k} + \frac{\delta}{\delta x_j}[\Gamma_\epsilon \frac{\delta\epsilon}{\delta x_j}] \tag{5.5}$$

with

$$\Gamma_k = \mu + \frac{\mu_t}{\sigma_k} \tag{5.6}$$

$$\Gamma_\epsilon = \mu + \frac{\mu_t}{\sigma_\epsilon} \tag{5.7}$$

In these equations, P_k, represents the generation of turbulent kinetic energy due to the mean velocity gradients

$$P_k = \mu_t\left(\frac{\delta U_i}{\delta x_j} + \frac{\delta U_j}{\delta x_i}\right)\frac{\delta U_i}{\delta x_j} + \frac{2}{3}\rho k\delta_{ij}\frac{\delta U_i}{\delta x_j} \tag{5.8}$$

$C_{\epsilon 1}$, $C_{\epsilon 2}$, σ_k and σ_ϵ are constants.

The eddy or turbulent viscosity, μ_t, is computed by combining k and ϵ as follows

$$\mu_t = C_\mu \rho \frac{k^2}{\epsilon} \tag{5.9}$$

where C_μ is a constant. The turbulent stresses are computed from

$$\rho \overline{u_i u_j} = -\mu_t \left(\frac{\delta U_i}{\delta x_j} + \frac{\delta U_j}{\delta x_i} \right) + \frac{2}{3} \rho k \delta_{ij} \tag{5.10}$$

The dispersed phase zero equation model a turbulent Prandtl number relating the dispersed phase kinematic eddy viscosity to the continuous phase kinematic eddy viscosity.

$$v_{td} = \frac{v_{tc}}{\sigma} \Rightarrow \mu_{td} = \frac{\rho_d}{\rho_c} \frac{\mu_{tc}}{\sigma} \tag{5.11}$$

where σ is a turbulent Prandtl number, v_{td} is the dispersed phase kinematic eddy viscosity, and v_{tc} the continuous phase kinematic eddy viscosity.

5.1.7 Near wall treatment

An important issue in the accurate prediction of turbulent flows is the formulation and the numerical treatment of the equations in regions close to solid walls. The near wall formulation determines the accuracy of the wall shear stress and the wall heat transfer predictions and has an important influence on the development of boundary layers, including the onset of separation.

Typically the two following approaches are used to model the flow in the near-wall region:

- The wall-function method
- The low-Reynolds number method

The wall-function approach used in this thesis is an extension of the method of Launder and Spalding [88]. In the log-law region, the near wall tangential velocity is related to the wall-shear stress, τ_ω, by means of a logarithmic relation.

In the wall-function approach, the viscosity affected sublayer region is bridged by employing empirical formulas to provide near-wall boundary conditions

for the mean flow and turbulent transport equations. These formulas connect the wall conditions (e.g. the wall-shear stress) to the dependent variables at the near-wall mesh node which is presumed to lie in the fully-turbulent region of the boundary layer.

The logarithmic relation for the near wall velocity is given by:

$$u^+ = \frac{U_t}{\mu_\tau} = \frac{1}{\kappa} ln(y^+) + C \tag{5.12}$$

where

$$y^+ = \frac{\rho \Delta y u_t}{\mu} \tag{5.13}$$

$$\mu_\tau = \left(\frac{\tau_\omega}{\rho} \right)^{1/2} \tag{5.14}$$

u^+ is the near wall velocity, u_τ is the friction velocity, U_t is the known velocity tangent to the wall at a distance of Δy from the wall, y^+ is the dimensionless distance from the wall, τ_ω is the wall shear stress, κ is the von Karman constant and C is a log-layer constant depending on wall roughness.

The idea behind the scalable wall function is to avoid the limitations imposed by standard wall functions in terms of near-wall grid resolution. Typically, the near-wall grid spacing has to satisfy requirements of the form $y^+ > Y^+_{low}$, where $Y^+_{low} \approx 20$, depending on the numerical formulation. Particularly for the flows at low device-Reynolds numbers, this is a severe limitation, as the boundary layer can be quite thin so that it cannot be resolved with a coarse near-wall grid.

The wall-function formulation can be explained for a cell-centered discretization, as shown in Figure 5.4.

The conservation equations are assembled by integration over control volumes. The fluxes are computed at the integration points. The missing flux at the wall must be supplied by the boundary condition. In case of wall functions, this is usually achieved by the application of a logarithmic profile assumption. It implies that the first grid point (i=1) lies in the logarithmic part of the boundary layer.

This boundary layer relation is only correct if the first grid point (i=1) lies in the logarithmic region. In case of a fine near-wall grid, the restriction is violated and the wall function accuracy will deteriorate. Eventually, the formulation will become singular as $y^+ \to 0$. For the flow of low Reynolds numbers, the extent of the logarithmic layer is much reduced and it becomes

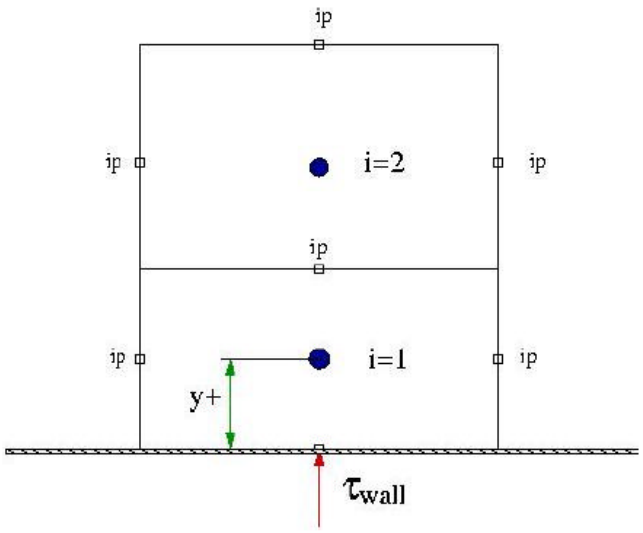

Figure 5.4: *Near-wall grid for cell-centered discretization*

increasingly difficult to place the first grid point in that region. Even if this can be achieved, it would in most cases result in an under-resolved boundary layer.

5.1.8 Interphase drag

For low Mach number flows, the drag exerted on an immersed body by a moving fluid arises from two mechanisms only. The first is due to the viscous surface shear stress, and is called skin friction. The second is due to the pressure distribution around the body, and is called the form drag. The total drag force can be expressed in terms of the dimensionless drag coefficient, C_D.

For a particle of simple shape, immersed in a Newtonian fluid and which is not rotating relative to the surrounding free stream, the drag coefficient, C_D, depends only on the particle Reynolds number. The function C_D (Re_α) may be determined experimentally, and is known as the drag curve [43].

One commonly used drag model for densely distributed solid particles is the Wen Yu Drag Model [89]. The Wen Yu correlation is valid for solid volume fractions at least up to 0.2. The drag coefficient is defined as:

$$C_D = \phi_c^{-1.65} max\left(\frac{24}{Re'}(1 + 0.15Re'^{0.687}), 0.44\right) \tag{5.15}$$

Re' is defined as ϕ_cRe, ϕ_c is the continuous phase volume fraction.

For very dense gas-solid or liquid-solid flows, such as those that occur in fluidized bed applications, the Gidaspow correlation [90] can be used. This uses the Wen Yu correlation for low solid volume fractions $\phi_d < 0.2$, and switches to Ergun's law [91] for flow in a porous medium for larger solid fractions.

$$c_{\alpha\beta}^{(d)} = 150\frac{(1-\phi_c)^2\,\mu_c}{\phi_c d_p^2} + \frac{7}{4}\frac{(1-\phi_c)\,\rho_c \mid U_c - U_d \mid}{d_p} \tag{5.16}$$

$\phi_c < 0.8$

The Gidaspow drag model is used in this setup.

5.2 Particle collision models

The CFD model used in this work was based on the extended two-fluid model [90]. Two different approaches to describe particle - particle interactions were simulated. The two different models are the kinetic theory of granular flow [90] and the Gidaspows solids pressure model [90].

In the kinetic theory of granular flow the particles are considered to be smooth, spherical, inelastic and undergoing binary collisions. The fundamental equations of mass, momentum and energy conservation are then solved for each phase.

The kinetic theory model for solids stress tensor is based on the kinetic theory of gases, generalized to take into account inelastic particle collisions. In these models, the constitutive elements of the solids stress are functions of the solid phase granular temperature, defined to be proportional to the mean square of fluctuating solid phase velocity due to inter-particle collisions

$$\Theta_s = \frac{1}{3}\overline{u_s'^2} \tag{5.17}$$

The kinetic theory model for solids pressure is similar to the equation of state for ideal gases, modified to take account of inelastic collisions and maximum solid packing.

$$P_s = \rho_s r_s \Theta_s \left(1 + 2\left(1+e\right) g_0 r_s\right) \tag{5.18}$$

Here, e denotes the coefficient of restitution for solid-solid collisions and g_0 (r_s) denotes the radial distribution function. The restitution coefficient, which quantifies the elasticity of particle collisions (one for fully elastic and zero for the fully inelastic), was taken as 0.9. The radial distribution function, g_0, can be seen as a measure of the probability of interparticle contact. Popular models for the radial distribution function are given by Gidaspow

[90].

$$g_0(\phi_s) = 0.6\left(1 - \left(\frac{\phi_s}{\phi_{sm}}^{\frac{1}{3}}\right)^{-1}\right) \tag{5.19}$$

where ϕ_{sm} is the volume fraction of a settled bed of solids. The g_0 function becomes infinite when the in situ solids volume fraction approaches ϕ_{sm}. A value of $\phi_{sm} = 0.55$ is chosen in this set up and is in accordance with experimental results [92].

In the solids pressure model the forces due to solid collisions are taken into account by introducing additional solids pressure and solids stress terms into the solid phase momentum equation based on the Gidaspow model [90].

The solids pressure force model can be used for dispersed solid phases in a multiphase flow. The forces due to solid collisions are taken into account by introducing additional solids pressure and solids stress terms into the solid phase momentum equations based on either the Gidaspow model or by specifying the elasticity modulus directly.

The collisional solids stress tensor in the solid phase momentum equation is defined as:

$$\tau_{sij} = -P_s\delta_{ij} + \mu_s\left(\frac{\partial U_i}{\partial x_j} + \frac{\partial U_j}{\partial x_i} - \frac{2}{3}\frac{\partial U_k}{\partial x_k}\delta_{ij}\right) + \zeta_s\frac{\partial U_k}{\partial x_k}\delta_{ij} \tag{5.20}$$

where P_s denotes solids pressure, μ_s denotes solids shear viscosity and ζ_S denotes solids bulk viscosity.

The most common equations for solids pressure are due to Gidaspow [90]. These specify the solids pressure gradient rather than solids pressure directly.

$$P_s = P_s\left(\phi_s\right) \Rightarrow \nabla P_s = G\left(\phi_s\right)\nabla\phi_s \tag{5.21}$$

$$G\left(\phi_s\right) = G_0 e^{c(\phi_s - \phi_{s,max})} \tag{5.22}$$

Where $G(\phi_s)$ is the elasticity modulus, G_0 is the reference elasticity modulus, c is the compaction modulus, and $\phi_{s,max}$ is the maximum packing parameter.

5.3 Maximum packing fraction

The maximum packing fraction, $\phi_{s,max}$, is the volume fraction of the solid phase at its state of maximum packing. For a dispersed solid phase the

maximum packing fraction may range from 0.5 to 0.74, the latter being the maximum possible packing for solid spheres [43]. The maximum packing fraction used in this study is 0.55 which where determined during the experiment [1] based on a routine suggested by Hoffmann and Finkers [93]. The maximum packing parameter is used in models for the particle collision forces.

5.4 Viscosity

The viscosity for the carrier phase was taken as the one for water at standard conditions, i.e 0.001 Pa s. The apparent viscosity of the dispersed phase was set to depend on the volume fraction of the solid. In this work the viscosity of the carrier phase was taken to be constant, independent of the solid phase concentration in the system. In order to account for the variation in the rheological behavior of the entire suspension with the solids concentration, the viscosity of the solid phase, μ_s was modified to the extent that the resulting viscosity of the suspension approximately agrees with that determined experimentally. This can be done by fitting experimentally determined suspension viscosity by the Roscoe-Brinkmann correlation [94] of the form

$$\frac{\mu_{susp}}{\mu_l} = (1 - \phi_s)^a \tag{5.23}$$

The relation was studied by Balakin et al. [92]. A good fit was obtained for a = -2.55. Assuming that the viscosity of the whole suspension is approximately given by: $\phi_s\mu_s + \phi_l\mu_l$, the solid viscosity can be found from:

$$\mu_s = \frac{\mu_l \left((1 - \phi_s)^a - \phi_l\right)}{\phi_s} \tag{5.24}$$

where μ_l is the viscosity of the continuous phase, ϕ_s is the volume fraction of the dispersed phase and ϕ_l is the volume fraction of the continuous phase.

The dependence of the solid viscosity as a function of the hydrate volume fraction is presented in Figure 5.5.

As can be seen from Figure 5.5 the viscosity goes to infinity at a packing fraction close to 1. In reality the suspension viscosity becomes infinite at the packing limit. A satisfactory model which correctly reflects that the suspension viscosity becomes infinite at the packing fraction, $\phi_{s,max}$, not a packing fraction of unity was derived by Krieger and Dougherty [95]. They considered that the viscosity increased due to adding particles to a suspension already containing particles.

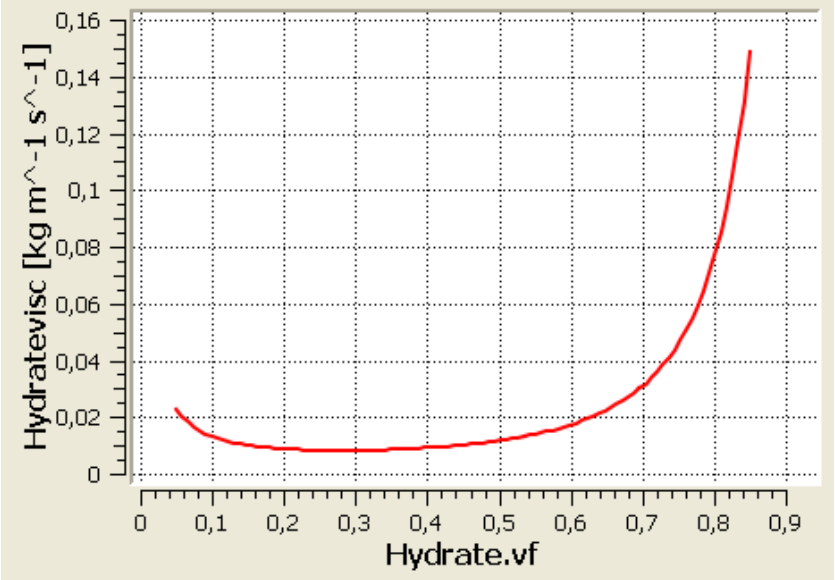

Figure 5.5: *Solid viscosity as a function of solid volume fraction. The curve is obtained from the expression based on the Roscoe-Brinkmann correlation [94].*

$$\frac{\mu_{susp}}{\mu_l} = \left(1 - \frac{\phi_s}{\phi_{s,max}}\right)^{a\phi_{s,max}} \tag{5.25}$$

resulting in the following expression for the solids viscosity needed to fit the suspension viscosity

$$\mu_s = \frac{\mu_l \left(\left(1 - \frac{\phi_s}{\phi_{s,max}}\right)^{a\phi_{s,max}} - \phi_l\right)}{\phi_s} \tag{5.26}$$

a was determined based on pressure drops in numerical simulations conducted by Balakin et al. [1]. The pressure drop in the flow of a uniform suspension (i.e. with a velocity high enough to have a uniform suspension) was matched to those determined experimentally in the flow loop, finding a value of a = -2.0.

The dependence of the solid viscosity as a function of the hydrate volume fraction is presented in Figure 5.6. As can be seen from Figure 5.6 the viscosity becomes infinite at the maximum packing fraction.

Both expressions for the solids viscosity were used in this study.

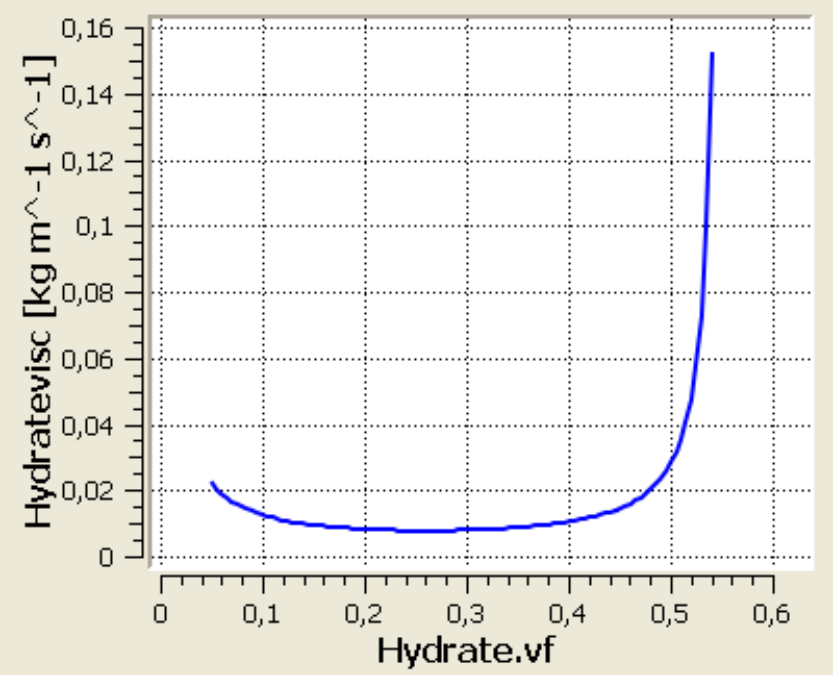

Figure 5.6: *Solid viscosity as a function of solid volume fraction. The curve is obtained from the expression derived by Krieger-Dougherty [95]*

5.5 Particle size

The particle size is significantly influenced by aggregation and breakage, related to shear in the flow [96]. From Balakin et al. [96] it was found that the particle size was not only the result of the hydrate particle evolution in the pipeline. The effect from the upstream feed pump is also important in terms of particle aggregation and breakage. The pump effect may both decrease and increase the average particle size in the system dependent on the level of agitation.

The particle size distribution was taken from Balakin et al. [1] where the particle size was set to be dependent of flow parameters and their cohesive properties according to the work of Mühle [97].

$$d_h = \left(\frac{F_a (d_1)^{2-fr}}{\mu_w \gamma} \right)^{\frac{1}{4-fr}} \tag{5.27}$$

where d_h is the hydrate aggregate diameter, γ the shear rate and some parameters determined by the series of population balance simulations: $d_1 = 7$ μm which is the diameter of the hydrate primary particle, $F_a = 1.75$ nN which is the floc adhesion force and $fr = 1.83$ which is the aggregate fractal

dimension.

The particle size as a function of the mean flow velocities is given in Figure 5.7.

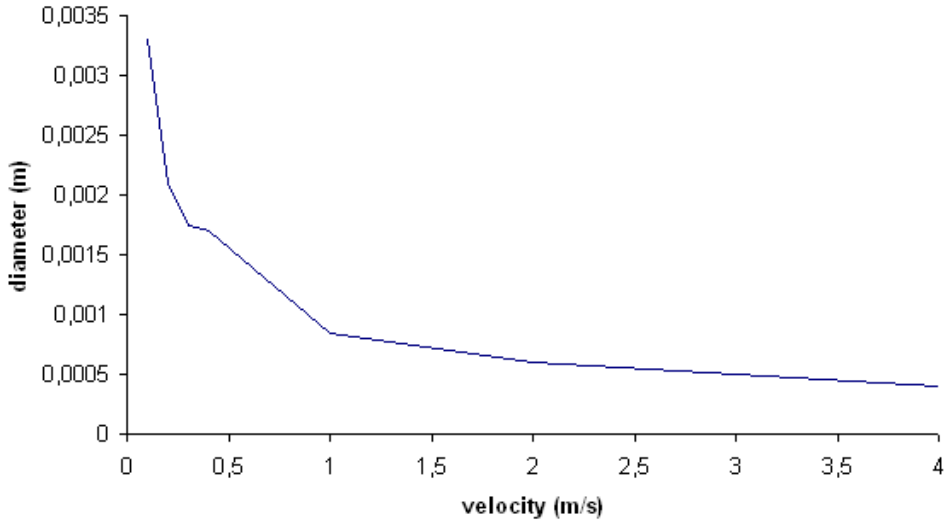

Figure 5.7: *Spatially averaged hydrate particle size as a function of mean velocity. The particle size is dependent of flow parameters and their cohesive properties according to the work of Mühle [97].*

5.6 Solver control

The high resolution advection scheme was chosen to calculate the advection terms in the discrete finite volume equations.

The Second Order Backward Euler was used as the transient scheme. The transient scheme defines the discretization algorithm for the transient term [85]. It is an implicit time-stepping scheme and is second-order accurate. When using the Second Order Backward Euler scheme, the transient scheme for turbulence equations will remain first-order, and the transient scheme for volume fractions will be set to a bounded second-order scheme.

5.7 The coupled solver

Segregated solvers employ a solution strategy where the momentum equations are first solved, using a guessed pressure and an equation for a pressure correction is obtained. Because of the guess-and-correct nature of the linear system, a large number of iterations are typically required in addition to the need for selecting relaxation parameters for the variables.

In ANSYS CFX, a coupled solver is used, which solves the hydrodynamic equations (for u, v, w, p) as a single system. This solution approach uses a fully implicit discretization of the equations at any given time step.

5.8 Timestepping

Timesteps are used to be able to track the real time progress during the simulations. The selection of an appropriate timestep size is essential in order to obtain good convergence. A too large timestep will lead to poor convergence and a too small timestep will lead to larger computational time. Within a given timestep the transport equations are solved during an iteratively process until the convergence criteria is met for all equations.

In these simulations a constant timestep of 0.002 s was used. Each timestep was considered to be converged when the maximum residual value was no higher than 1×10^{-5}.

Chapter 6

Results and discussion

Numerical simulations on hydrate deposition and bed formation in a horizontal pipe have been conducted using an Eulerian-Eulerian approach. The bed height has been measured for different inlet velocities and compared to experimental results and similar numerical simulations performed by a different software. Two different particle collisions models were used; kinetic theory of granular flows and Gidaspows solids pressure model. The effect of the solid viscosity was investigated as well as the effect of the particle diameter and wall boundary condition. The results from the simulations are presented and analyzed below.

6.1 Grid dependency

Grid dependency is a known problem in computational fluid dynamics and time dependent processes such as particle deposition will typically be affected. Grid dependency will reduce the predictive capabilities of the numerical solver and thus give varying results depending on the grid resolution. It is known that the numerical solution of the Navier-Stokes equations becomes more and more accurate if the grid is refined. However, the maximum grid resolution that is practically feasible is limited by the available computer power and time.

In the current work, grid dependency was assessed by repeating simulations with various grid resolutions. The grid resolution was varied up to a total of 150 000 elements. The solutions from the simulations did not change for grid resolutions over 70 000 elements. An example on how to check for grid independency is presented in Figure 6.1 where the velocity profile of the continuous phase on a midline cross-section of the pipe as a function of a dimensionless vertical coordinate is shown. The profile for three different

grid resolutions are plotted. It can be seen that the difference between the grids are negligible.

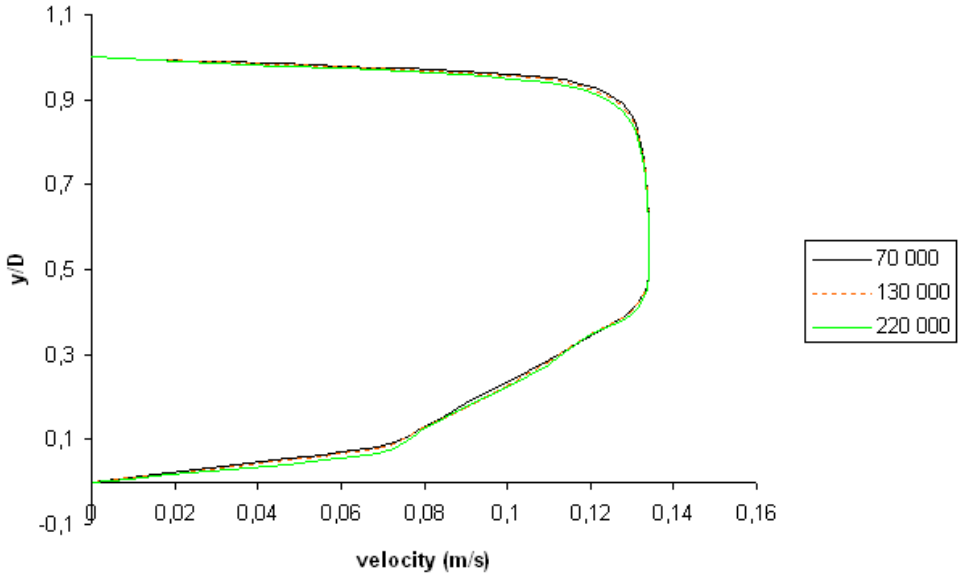

Figure 6.1: *Velocity profile of the continuous phase velocity on a midline cross-section of the pipe as a function of a dimensionless vertical coordinate for three different grid resolutions. Mean flow velocity 0.1 m/s.*

A grid with 70 552 elements, including five layers of inflation to encount the near wall behavior, was chosen due to limited computational power.

6.2 Hydrate bed formation simulations

Particle deposition is a process that plays a key role in many fields. In the oil and gas industry, the accumulation of hydrate is one of the most challenging aspects in flow assurance studies. Formation of a hydrate bed will increase the pressure drop and eventually even lead to plugging of the pipeline or process equipment, causing serious risk to the safety of operating personnel and equipment.

Because of simultaneous influences on fluid flow convection, particle-boundary interactions, particle-particle interactions, colloidal interactions, molecular diffusion and external body forces make particle deposition on a surface a complicated process. However, for larger particles, as used in this work, the

particle behavior is dominated by inertia and gravity. The particle deposition takes place when the gravity force becomes dominant compared to the combination of buoyancy and the drag force. Aggregation of particles will increase the mean particle size which will increase the deposition rate of the particles.

The introduction of bend and obstructions will also affect the deposition process. The velocity in a pipeline bend will be larger compared to the horizontal section. This can be seen in Figure 6.2, where the contour on the continuous phase velocity is presented for the pipe midline cross-section at 0.1 m/s. The particle concentration will be at a maximum of the outer section of the bend. This is due to the particles being centrifuged outwards in the bend. A contour presenting the hydrate volume fraction on a midline cross-section is shown in Figure 6.3. From the figure it can be seen that the hydrate bed is thicker in the bend compared to the horizontal section.

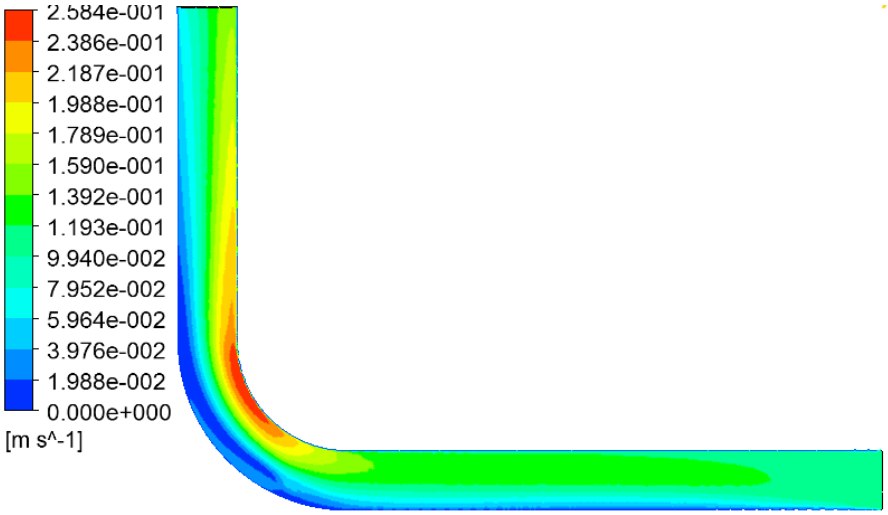

Figure 6.2: *Contour of the continuous phase velocity on a midline cross-section of the pipe. The maximum velocity is found in the inner part of the bend. The velocity in the lower horizontal region of the pipe is smaller due to the obstruction caused by the particle bed. Mean flow velocity 0.1 m/s.*

In the work by Doron et. al [54] three main flow patterns in solid-liquid flow were defined:

1. *Fully suspended flow* - at high flow rates all solid particles are suspended.

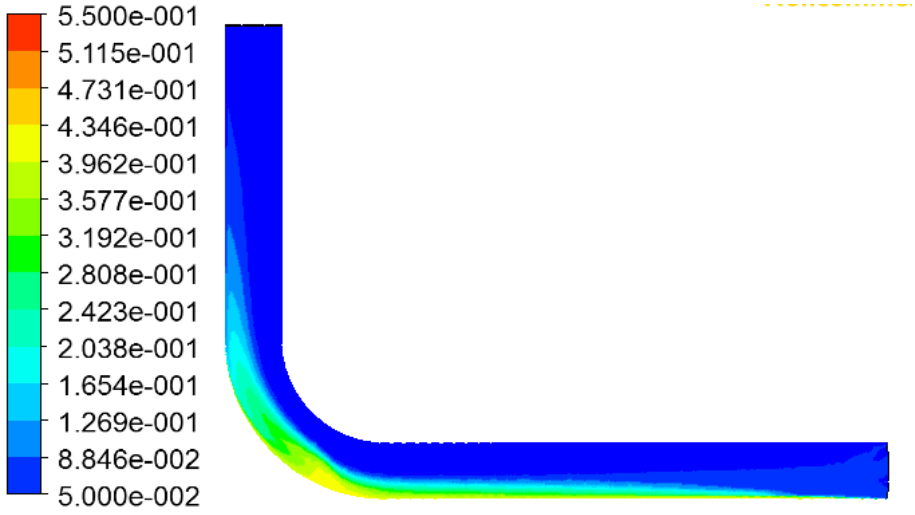

Figure 6.3: *Contour of the hydrate volume fraction at a midline cross-section of the pipe. Mean flow velocity 0.1 m/s.*

2. *Flow with a moving bed* - at lower flow rates solid particles accumulate at the bottom of the pipe. Thus, they form a packed bed layer, which moves along the pipe bottom.

3. *Flow with a stationary bed* - when the flow rate velocity is too low to enable motion of all immersed particles, a stationary deposit is observed at the bottom of the pipe. On top of this stationary layer particles are transported as a separate moving layer.

Schematic views of the three main flow patterns are presented in Figure 6.4.

The hydrate bed measured from the simulations performed in this work is taken at the upper boundary of the moving bed. The method to determine the upper boundary of the moving bed is based on a ongoing work by Boris Balakin [98]. In this work the terminal velocity of particle deposition in each computed volume fraction layer was determined with the empirical correlation of Richardson and Zaki [99]:

$$u_t = \frac{1}{18}\frac{(\rho_s - \rho_l)}{\mu_l} d^2 g \left(1 - \phi_s\right)^5 \tag{6.1}$$

where u_t is the terminal velocity of the settling particle. The settling is mostly hindered at the lower layer of the deposits while there is an increase in the terminal velocity in the transition region leading to the slurry phase in the pipe. Figure 6.5 presents the hydrate volume fraction and mean terminal

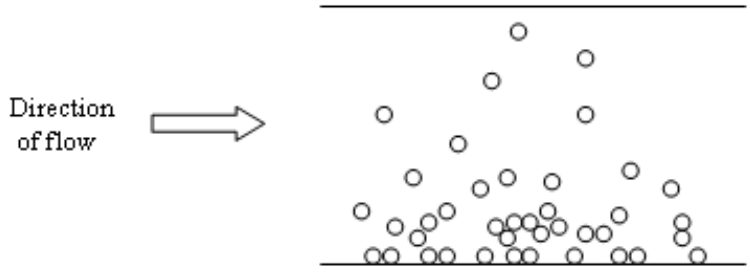

(a) Heterogeneous suspension flow

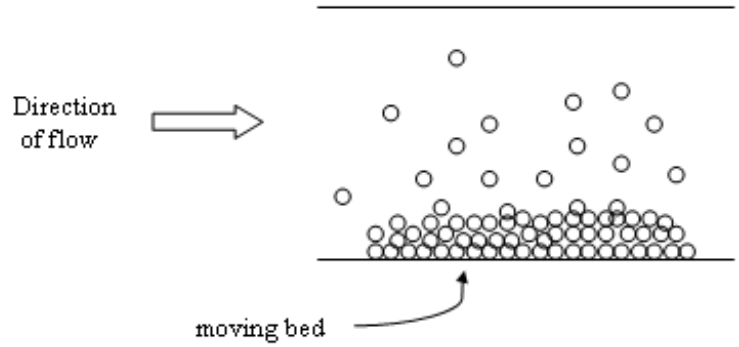

(b) Flow with at moving bed

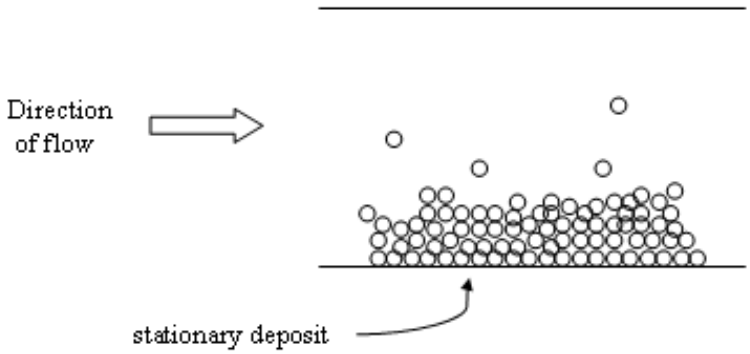

(c) Flow with a stationary bed

Figure 6.4: *Schematic views of flow patterns and concentration distributions in a direction perpendicular to the pipe axis.*

velocity of settling particles in the near-wall subsurface as a function of a dimensionless vertical coordinate.

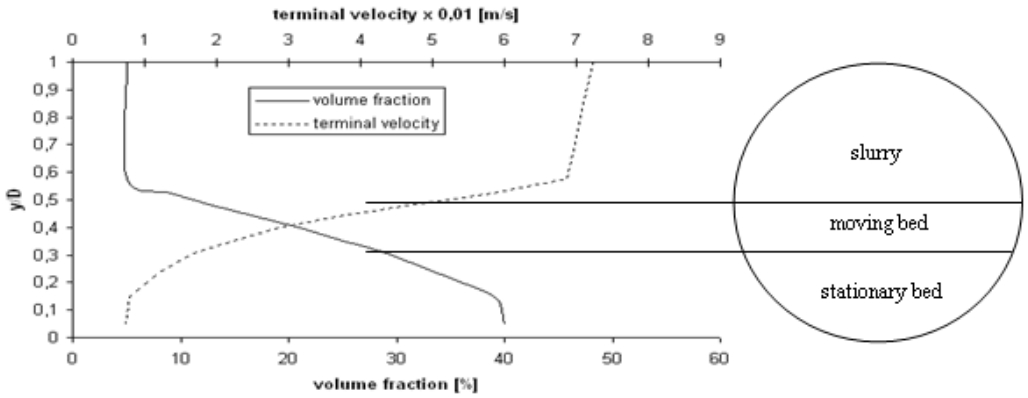

Figure 6.5: *Hydrate volume fraction and mean terminal velocity of settling particles as a function of dimensionless vertical coordinate. Mean flow velocity 0.1 m/s.*

Hydrate particles, located in the region above the transition point, change the direction of their movement from the vertical deposition to axial flow in the stream direction, sliding on the surface of the lower bed layers. It is confirmed by the results from the simulations, that the vertical component of the flow velocity is at the minimum in this region. This zone is defined as an upper boundary of the moving bed and is used to define the upper boundary of the hydrate bed in the numerical simulations.

Balakin et al. [92] reported that in the experiment with hydrate volume fractions in the interval 0.05 - 0.1 did not affect the flow properties much (e.g. pressure drop) at high mean flow velocities. However, when the mean velocity was decreased below 0.4 m/s particles began to settle, producing visible regions of higher concentration in the bottom of the horizontal segments of the pipeline. At higher velocities the hydrate particles were homogeneously dispersed in the continuous phase.

Transient simulations with inlet velocities in the region 0.1 - 1 m/s with hydrate volume fraction at 0.05 were performed to try to reproduce the bed formation results from the experiments. Both the kinetic theory of granular flows and Gidaspows solids pressure model were used in the simulations.

At velocities larger than 0.4 m/s there were no hydrate bed formation in the horizontal section. From Figure 6.6, presenting the hydrate volume fraction in the near wall region, one can see that there is no bed formation in the pipe. The hydrate is homogeneously dispersed in the continuous phase.

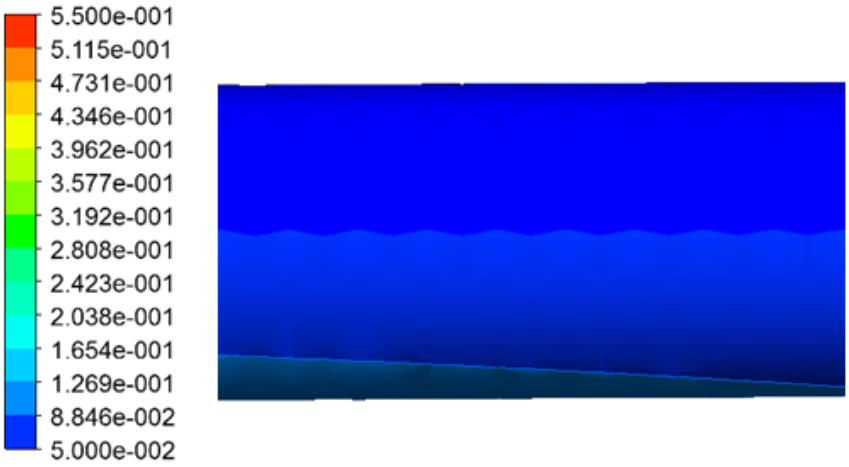

Figure 6.6: *Contour plot of the hydrate volume fraction in the near wall region. Mean flow velocity; 0.5 m/s, hydrate volume fraction; 0.05, mean particle size; 165 μm.*

Decreasing the inlet velocity below 0.4 m/s causes decrease in the particle slip velocity and in the turbulent mixing of the particles compared with the net force of gravity. This leads to the development of compaction of the hydrate particles in the bottom zones of the horizontal pipeline section. This effect is shown in Figure 6.7, which presents the particle concentration in the near wall subsurface of the pipeline using Gidaspows solids pressure model. The figure also shows that the hydrate bed is increased at decreasing velocity.

The contours given in Figure 6.7 are created using 14 colors in the range 0.05 - 0.55 hydrate volume fraction, where 0.55 is the maximum packing limit. Each color denotes a specific volume fraction range.

Figure 6.8 is a close up of Figure 6.7b which focuses on the horizontal region. In the figure the hydrate volume fraction at the wall is better visualized. The top 4/10 of the pipe has a packing less than 0.1 and it is clearly a freeboard over the bed. The lower part of the bed shows an increasing volume fraction towards the bottom of the pipe. The bed has a maximum packing fraction of approximately 0.4. The results from the simulations at different mean

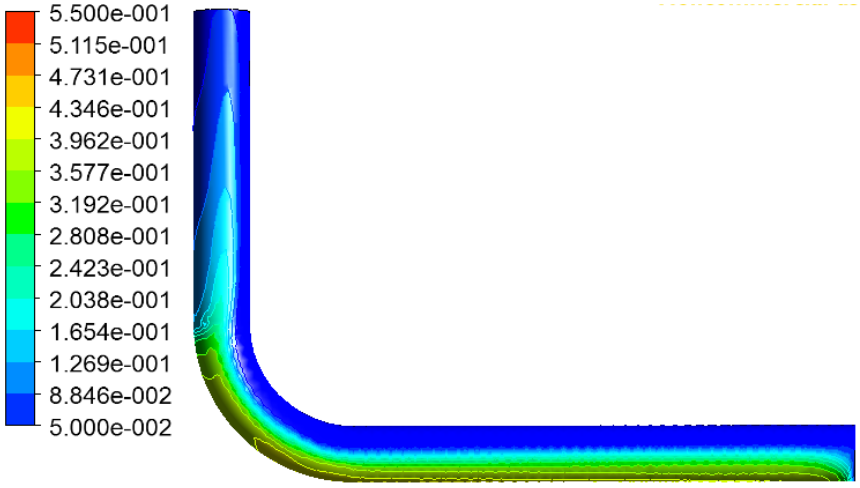

(a) 0.1 m/s mean flow velocity

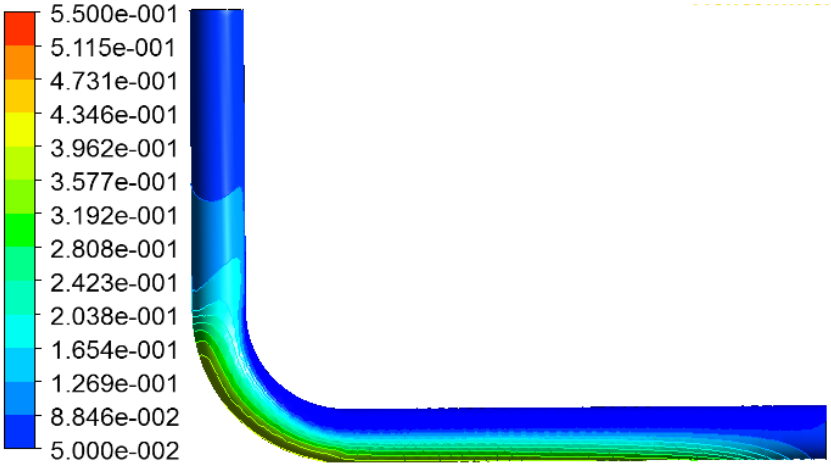

(b) 0.2 m/s mean flow velocity

Figure 6.7: *Contour plots of hydrate volume fraction near the wall. Mean flow velocities; 0.1 - 0.4 m/s, hydrate volume fraction; 0.05, hydrate particle size; 170 - 330 µm. The contours are taken from simulations using the solids pressure model.*

velocities show a maximum hydrate volume fraction in the range of 0.4-0.5.

During the experiment, hydrate bed thickness on the wall of the pipe was defined on the base of visual observations using a standard scale length-measurement device as shown in Figure 6.9. A similar figure can be produced from the simulations showing how the hydrate volume fraction on a midline

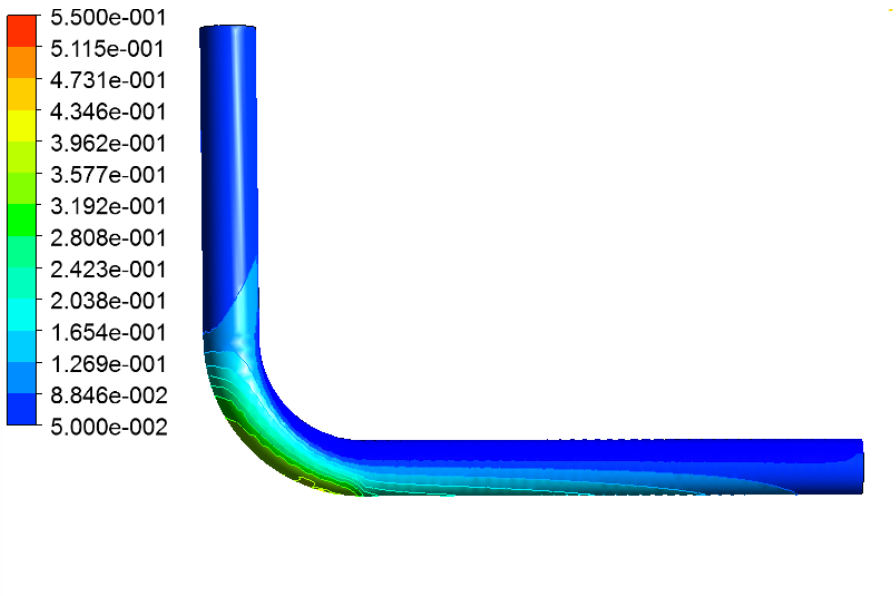

(c) 0.3 m/s mean flow velocity

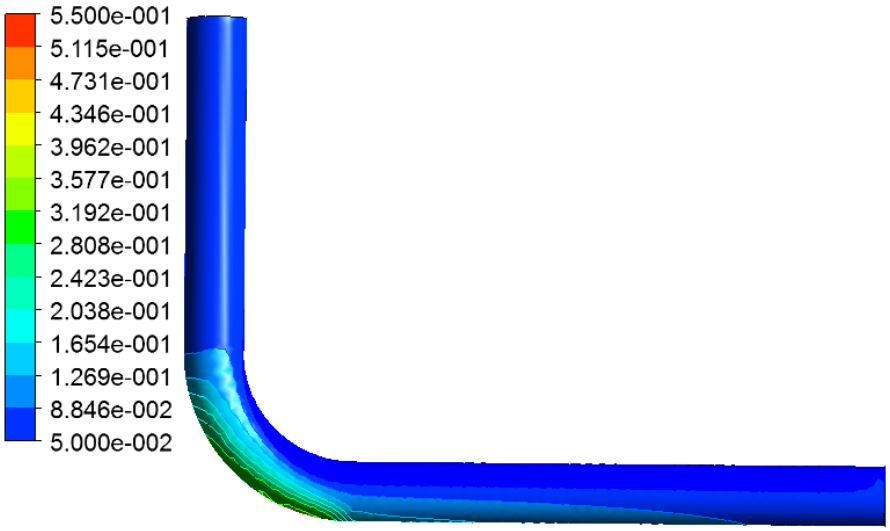

(d) 0.4 m/s mean flow velocity

Figure 6.7: *Contour plots of hydrate volume fraction near the wall. Mean flow velocities; 0.1 - 0.4 m/s, hydrate volume fraction; 0.05, hydrate particle size; 170 - 330 µm. The contours are taken from simulations using the Solids pressure model.*

cross-section of the pipe is distributed at a mean flow velocity of 0.1 m/s. The hydrate bed is more dense at the bottom of the wall. It can also be seen from Figure 6.10 that it is clear that the hydrates are deposited along the pipewall.

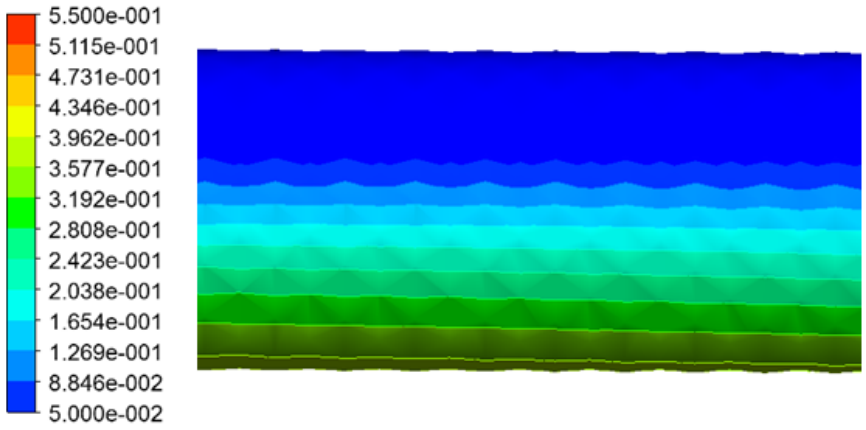

Figure 6.8: *Contour plot of the hydrate volume fraction showing a close-up of the horizontal pipe region. Mean flow velocity; 0.2 m/s, mean particle diameter; 210 μm.*

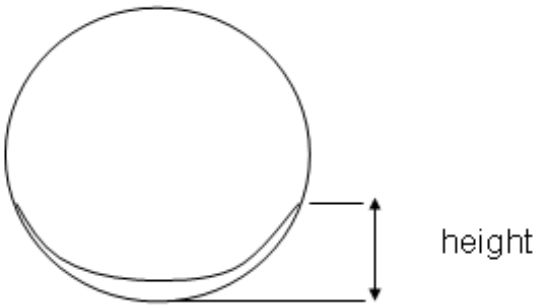

Figure 6.9: *A cross section of the pipe visualizing how the bed height was measured in the experiment performed by Balakin et al. [4].*

Figure 6.11 and Figure 6.12 present photographs of stable hydrate beds formed at a flow velocity of 0.28 and 0.1 m/s respectively. It can be seen from the figures that the slurry in this case is stratified into two zones of different particulate phase concentrations. It was also noted by the authors that the most dense region in the bottom part of the pipe was separated into two smaller zones with different behavior of the particulate phase. The lowest zone can be classified as a stationary bed with small-magnitude stochastic particle velocity fluctuations [100]. The second part, which was located in between the stationary bed and the homogeneous slurry, was determined as

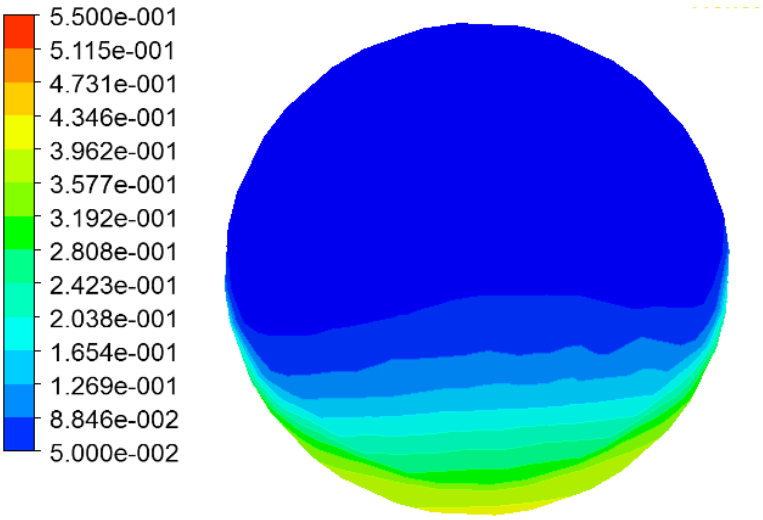

Figure 6.10: *A contour of hydrate volume fraction on a midline cross-section of the pipe at a mean flow velocity of 0.1 m/s.*

a moving bed [100], having particle velocity comparable to the one in the homogeneous flow pattern. In Figure 6.12 there is a sharper concentration gradient between the bed and the homogeneous suspension. This behavior was only seen at very low flow velocities. The predictive capabilities of CFX with respect to the concentration gradient as a function of the mean flow velocity is investigated later in this work.

Figure 6.11: *Hydrate bed in horizontal section of the loop. Mean flow velocity 0.28 m/s. Adopted by courtesy of Boris Balakin.*

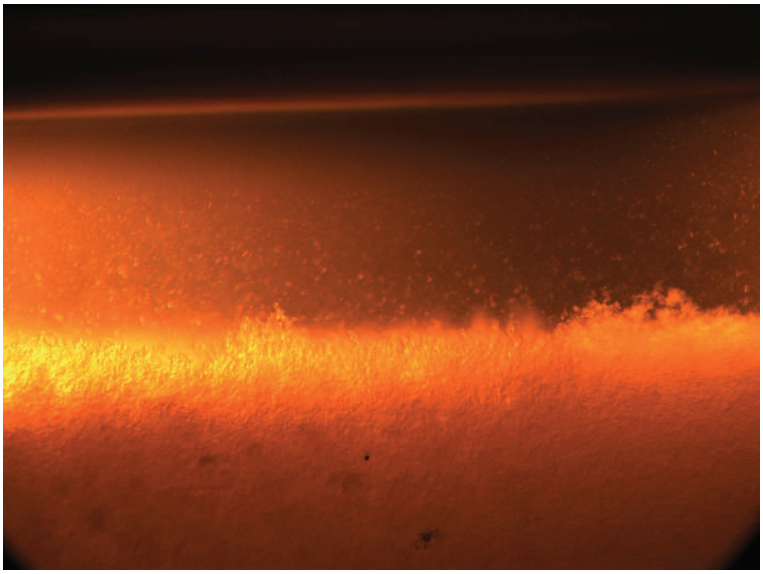

Figure 6.12: *Hydrate bed in horizontal section of the loop. Mean flow velocity 0.1 m/s. It can be seen from the photograph that the slurry is stratified into two zones of very different particulate phase concentrations. Adopted by courtesy of Boris Balakin.*

The thickness of the hydrate bed was determined experimentally measuring the distance between the pipeline bottom and the upper boundary of the sliding bed. During the experiment neither the volume fraction at the upper boundary nor the continuous phase velocity was measured at the upper boundary of the particle bed.

6.2.1 Kinetic theory of granular flows

Performing transient simulations using the kinetic theory to model the particle-particle collisions were challenging. The hydrate volume fraction in the lower part of the pipe reached unphysical large values (nearly 1) in the deposited layers. One possible reason for this is because the coupling between the pressure force on the solid at high packing fractions is not fully linearized with respect to changes in volume fraction for the kinetic theory model used in CFX. A contour of the hydrate volume fraction at the wall and on a midline cross-section of the pipe is presented in Figure 6.13. The red color denotes the maximum packing fraction, i.e 0.55. The hydrate bed did neither get dispersed at velocities higher than 0.4 m/s.

Several improvements were done to try to converge the kinetic theory model.

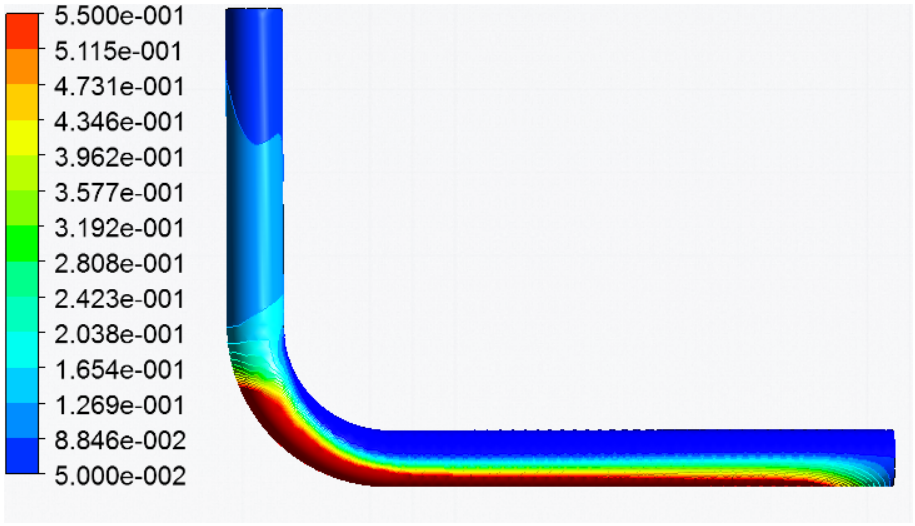

(a) Near-wall contour at a mean flow velocity of 0.2 m/s

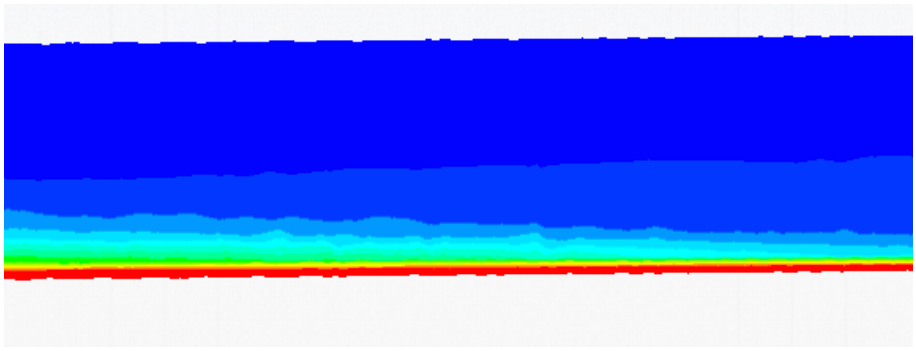

(b) Midline cross-sectional contour at a mean flow velocity of 0.2 m/s

Figure 6.13: *Contour plots showing the hydrate volume fraction. Initial set up using the kinetic theory model. The hydrate volume fractions in the bed reach unphysically high values.*

The buoyancy in Rhie-Chow and a buoyancy expert parameter were included. The Rhie-Chow term in the momentum equation was included to avoid "checker boarding" in the solution of the pressure when all the variables are located at the same point (at the vertices in the case of CFX). The body force that arises from buoyancy with other forces in Rhie-Chow can sometimes make the solution more robust. The buoyancy expert parameter treats the buoyancy term implicitly when this will improve the stability (by increasing the diagonal term in the matrix to be inverted) and does not if the flow is unstably stratified and the linearisation would destabilize the solution. Also, a CCL (CFX command language) command was included to define when the solids pressure force was applied. This is used to avoid

unphysically large solid fractions. The parameter was set to 0.4 which is approximately 30% less than the maximum packing fraction. These modifications led to convergense for simulations using inlet velocities in the range 0.2 - 0.4 m/s. Hydrate volume fractions at the wall and on a midline cross-section is shown in Figure 6.14 and 6.15 respectively.

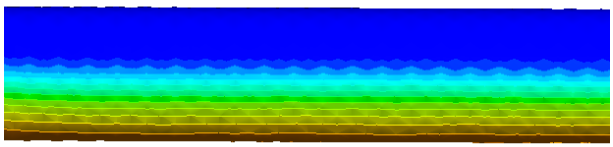

(a) Mean flow velocity 0.2 m/s

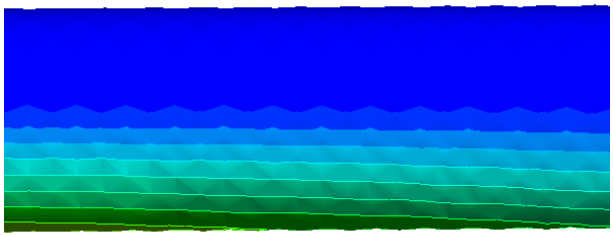

(b) Mean flow velocity 0.3 m/s

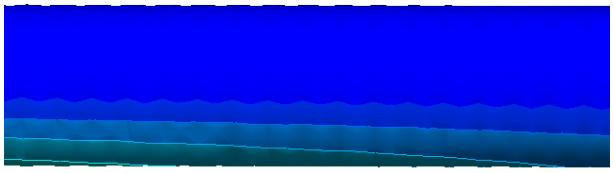

(c) Mean flow velocity 0.4 m/s

Figure 6.14: *Contour plots of the hydrate volume fraction in the near wall region in the horizontal section. Mean flow velocities 0.2 - 0.4 m/s, hydrate volume fraction 0.05, hydrate particle size 175 - 330 μm. The contours are taken from simulations using the kinetic theory model. The hydrate concentration is reduced at increasing velocities.*

Even though much effort was made in trying to converge the simulations for inlet velocities below 0.2 m/s this did not succeed. The simulations with larger inlet velocities show a tendency of oscillations in the residuals between 1×10^{-5} - 1×10^{-6}. Convergence is still met since the convergence criterion is 1×10^{-4}. The results also show a hydrate volume fraction in the bend

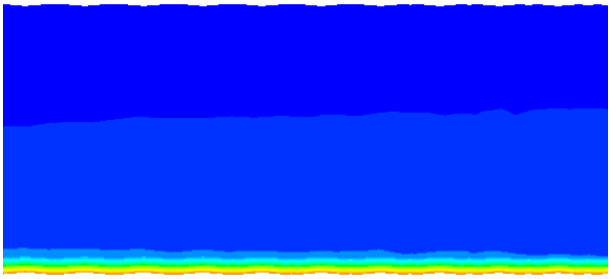

(a) Mean flow velocity 0.2 m/s

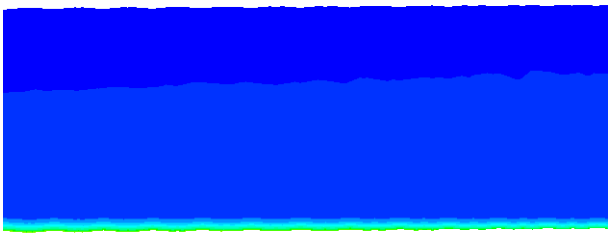

(b) Mean flow velocity 0.3 m/s

(c) Mean flow velocity 0.4 m/s

Figure 6.15: *Contour plots of the hydrate volume fraction on a midline cross-section of the pipe in the horizontal section. Mean flow velocities; 0.2 - 0.4 m/s. The contours are taken from simulations using the kinetic theory model. The vertical height of the bed is small and is further reduced at increasing velocities.*

close to the maximum packing fraction. It is believed that the reason for the solver crash in simulations below 0.2 m/s is due to the lack of linearisation of the coupling between the pressure force on the solid with respect to changes

in volume fractions. At lower velocities the bed will get more packed. Even though the CCL-command was included to define when the solid pressure is applied, it does not avoid the hydrate bed to reach high hydrate volume fractions creating convergence problems for the solver.

6.2.2 Gidaspow solids pressure model

Due to lack of linearisation and convergence problems for the kinetic theory model a new setup using Gidaspow solids pressure model was built. The coupling between the pressure force on the solid at high packing fractions is linearized with respect to changes in volume fraction. The linearisation is new for the solids pressure model and it was stated from ANSYS CFX Support that the solids pressure model was not yet validated. As for the kinetic theory setup the buoyancy in Rhie-Chow and a buoyancy expert parameter were included and the CCL command to define when the solids pressure force was applied.

Simulation at inlet velocities in the range 0.1 - 1 m/s gave satisfactory convergence. As for the kinetic theory model particle bed formation occurs at velocities lower than 0.4 m/s.

The contours giving the hydrate volume fraction at the wall are given in Figure 6.7. Contours of a midline cross-section in the horizontal section are presented in Figure 6.16. The contours show a clear dependence between the mean flow velocity and bed thickness. From the contours of the midline cross-section the vertical bed thickness is small even at low velocities. At higher than 0.3 m/s the bed cannot be seen on the contour. The figures show that the compacted regions are located along the pipeline wall and that the particle concentration in the central part of the cross-section is relatively smaller.

Figure 6.17 shows the measured hydrate bed as a function of the inlet velocity. The bed height decreases at larger mean flow velocities.The hydrate volume fraction in the bed does not exceed 0.55, which is caused by the solid pressure force effect.

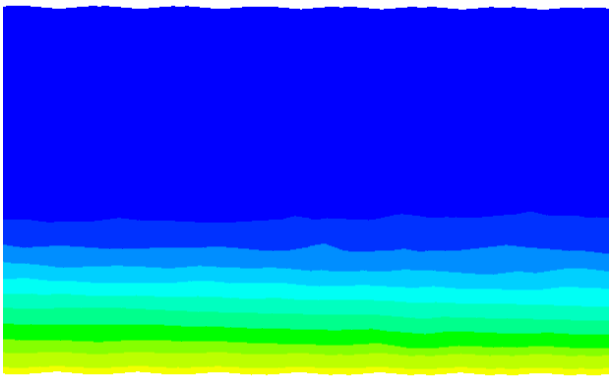

(a) Mean flow velocity 0.1 m/s

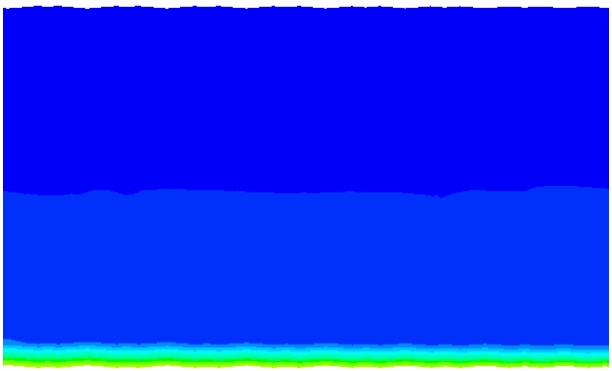

(b) Mean flow velocity 0.2 m/s

Figure 6.16: *Contour plots of the hydrate volume fraction on a midline cross-section of the pipe in the horizontal section. Mean flow velocities; 0.1 - 0.4 m/s. The contours are taken from simulations using the Gidaspow solids pressure model.*

(c) Mean flow velocity 0.3 m/s

(d) Mean flow velocity 0.4 m/s

Figure 6.16: *Contour plots of the hydrate volume fraction on a midline cross-section of the pipe in the horizontal section. Mean flow velocities; 0.1 - 0.4 m/s. The contours are taken from simulations using the Gidaspow solids pressure model.*

6.2.3 Comparison of the kinetic theory of granular flows and solids pressure model

Due to the linearisation of the solids pressure model it gave better convergence than the kinetic theory model. In Figure 6.17 the bed thickness versus inlet velocity is shown for both models. It can be seen that the two different setups give satisfactorily agreement. It would be interesting to have results from the kinetic theory setup at velocities lower than 0.1 m/s to see if it follows the solids pressure model.

Due to better convergence for the solids pressure model the results from this model have been used in the rest of this thesis.

6.3 Comparison with experimental results

The results from this study were compared with experimental results generated in an experimental rig filled with water-hydrate mixture [4]. The hydrate bed thickness predicted by the solids pressure model is presented in Figure 6.17 as a function of the mean flow velocity, and compared with experimental results. From the experiment it was observed that the bed is lifted up when the flow velocity was increased generally between 0.1 - 0.35 m/s. After this interval, the flow pattern became homogeneously mixed [4]. This tendency is also clear in the bed thickness predicted by the model. Even though the results from the model show the same tendency as the results from the experiments, the simulated results are not in total agreement with the experimental data. Reasons for disagreement between the model and experimental data can be due to:

- Geometry. The flow in the test section may have been influenced by the pump. The use of uniform velocity distribution may have resulted in less accurate simulations.
- Deposition of hydrate particles in the unmodelled part of the experimental rig.
- Not optimal selection of the hydrate-hydrate adhesion force which may cause an underprediction of the actual particle size.

It was also found that the bed growth did not correspond to what was observed during experiments. According to the experiments the time to form the bed was in the range of 30 seconds. The bed formation in these simulations was quite rapid. After approximately 10 seconds (depending on the inlet velocity) the bed size was constant. After this time the bed in the horizontal pipe did not change in height or concentration. Thus, most simulations

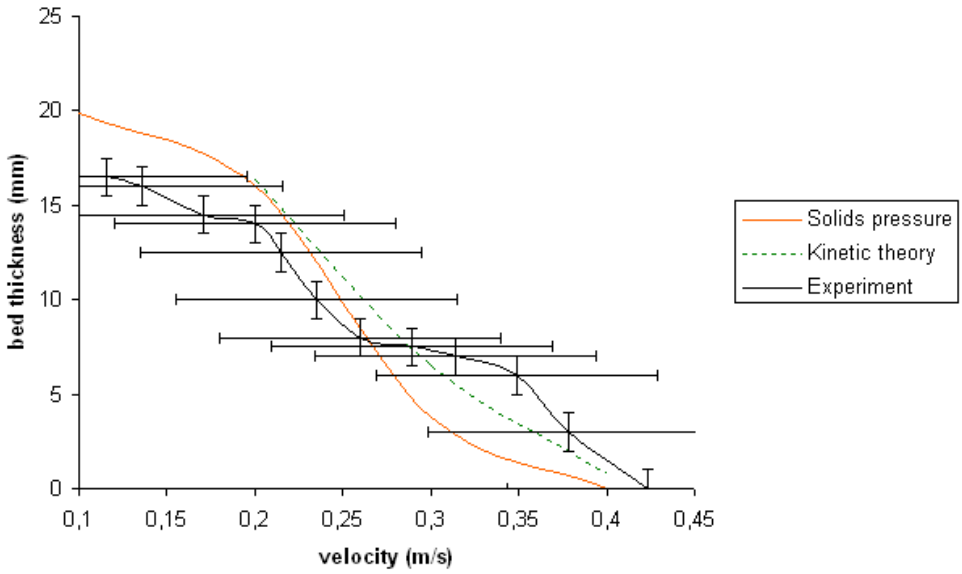

Figure 6.17: *Bed thickness as a function of mean flow velocities. Comparison of the Gidaspow solids pressure model and data obtained from experiment.*

performed has been stopped after approximately 10 - 15 seconds, to limit the computational time. A possible reason for the rapid bed growth can be due to the use of the turbulent dispersion force. When the turbulent dispersion force is not used then the hydrate will accumulate quickly because there is no dispersion process to remove the hydrate from the wall layer. When the turbulent dispersion is included then the deposition process must "compete" against the dispersion and it may take longer for the hydrate to accumulate. A sensitivity on the hydrate dispersion force is done and discussed later in Chapter 6.5.5.

6.4 Comparison with numerical studies

Balakin et al. [1] performed a numerical study of the hydrate bed formation using the commercial software STAR-CD and compared the results to the data from [4]. The simulation results were in qualitative agreement with experimental data. The multiphase flow was modelled with the Eulerian-Eulerian two-fluid model. The $k - \epsilon$ two-equation model was used for calculations of the turbulent stress tensor and the solids pressure model was used to model the particle-particle collisions.

The results obtained by Balakin et al. [1] are presented in Figure 6.18 and compared to data obtained by this study and the experimental results. Both softwares used the solids pressure model and an expression for the solid viscosity. From Figure 6.18 it can be seen that the bed thickness predicted by the different softwares is in qualitatively good agreement. Both softwares predict decreasing bed thickness at increasing flow velocities. At low flow velocities CFX predicts a higher bed thickness than STAR-CD, but at higher velocities CFX predicts a smaller bed thickness. Compared to the experimental results it is clear that STAR-CD has a better fit. STAR-CD is able to predict bed thicknesses in good agreement over the whole velocity range. CFX seems to overpredict the bed thickness at low velocities and under predict the bed thickness at higher flow velocities.

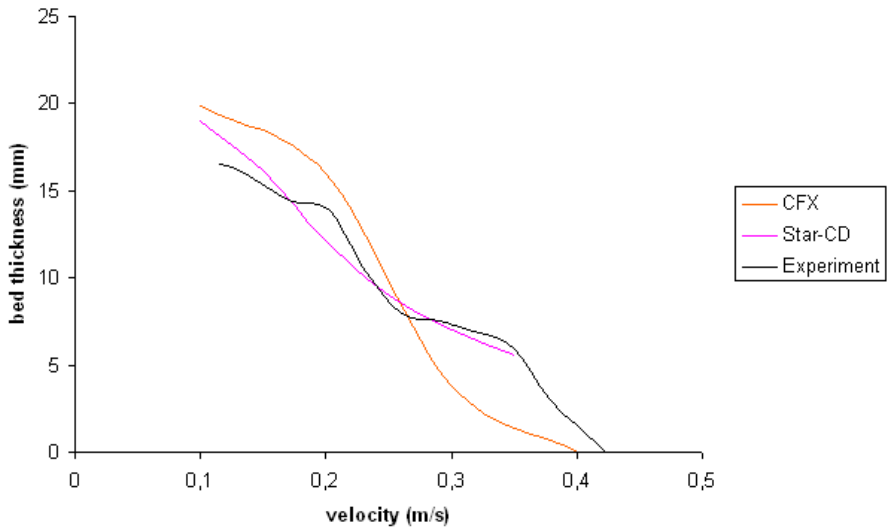

Figure 6.18: *Bed thickness as a function of mean flow velocity. Comparison of CFX and STAR-CD.*

The differences in the results between the two softwares can be due to:

- grid generation
- discretization
- geometry
- model set-up
- solver

The resolution of the grid in the two models is different, which could lead to differences in results between the models. The difference due to grid resolution is assumed to be small. Another possible reason for difference in the results is the discretization and how the solvers solve the transport equations. Both softwares are based on the finite volume method and the solvers are both coupled solvers. The solver in STAR-CD is based on SIMPLE (Semi-Implicit Method for Pressure-Linked Equations). In the SIMPLE algorithm the velocity and pressure equations are solved consecutively. In CFX's coupled solver, the velocity and pressure are solved simultaneously. This helps to reduce the numerical diffusion introduced by SIMPLE. Another difference is the advection scheme. The upwind scheme is used in the model in STAR-CD while the high resolution scheme is used in CFX. It is not very likely that these contribute heavily to the differences in the results between the softwares. STAR-CD gives better results even though the solver and advection scheme used in CFX should decrease the numerical errors compared to STAR-CD.

The geometry used in the two models is not equal. In this work only the test section with an upward facing bend is modelled. In the work by Balakin [1] the piping from the pump to the flowmeter was modelled. This included two more bends upstream the test section than what was modelled in this work. In the experimental set-up the total length of the straight pipeline after the pump was not enough to establish fully-developed turbulent flow, thus the flow pattern in the entire model may be influenced by the presence of the pump. It was therefore assumed that using a uniform velocity profile through the inlet of the test section would result in less accurate simulations, and a curved section before the inlet to the test section with the same radius as the pump was included to minimize the effect on the flow.

Differences in the set-up can also cause differences. In the work by Balakin [1] the turbulent dispersion force was enabled while in this current study it was not. It was done a sensitivity in this work to study the effect of the turbulent dispersion force. In CFX enabling the turbulent dispersion force led to a drastic decrease in bed thickness. Even at low mean flow velocities the maximum packing in the bed was heavily reduced. Experience from similar simulations in STAR-CD did not show this effect. The analyze of the model sensitivity is described further below.

6.5 Model sensitivity

Several sets of simulations were performed to do sensitivity analysis of different parameters to verify their effect on the hydrate particle bed. Sensitivities

were done for the solid viscosity, hydrate particle size and wall boundary conditions.

6.5.1 Effect of solid viscosity

The model allows to set a constant viscosity for the dispersed solid or include an expression for the viscosity directly. Two different expressions for the solid viscosity, as explained in Chapter 5.4, are used. The expression derived by Krieger and Dougherty [95] are the most correct physically since it reflects that the viscosity becomes infinite at the packing limit. Comparison of the bed thickness for simulations of the two different viscosity expressions is shown in Figure 6.19. The differences in results between the two viscosity expressions are negligible.

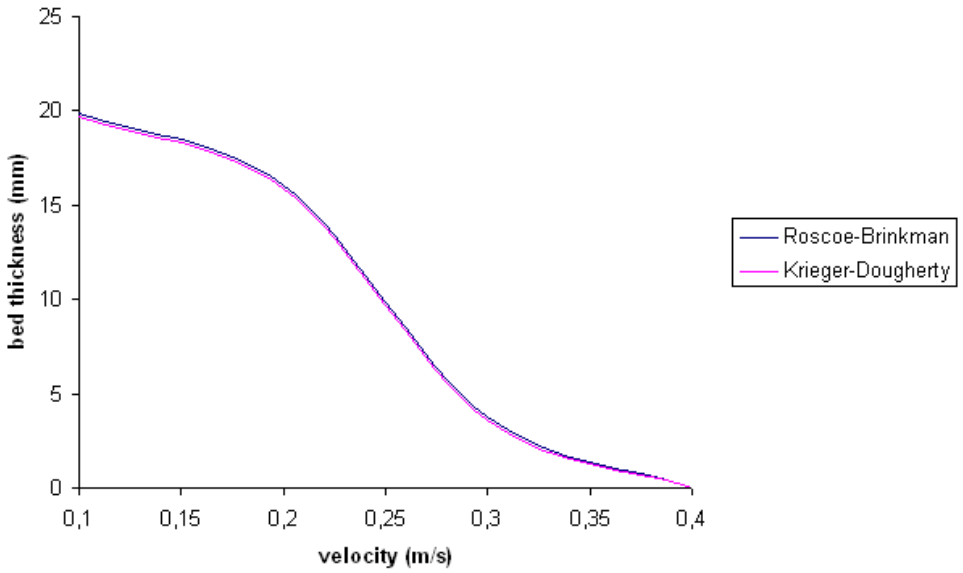

Figure 6.19: *Comparison of the different expressions for the solid viscosity. The blue dots represent the expression derived by Roscoe-Brinkmann [94] and the red dots represent the expression derived by Krieger-Dougherty [95].*

The viscosity in the near-wall region for a simulation with mean flow velocity of 0.2 m/s is presented in Figure 6.20 for the two different expressions for the solid viscosity.

A sensitivity to study the effect of the solid viscosity was performed. Different constant viscosities for the solid were chosen and simulated at a mean flow

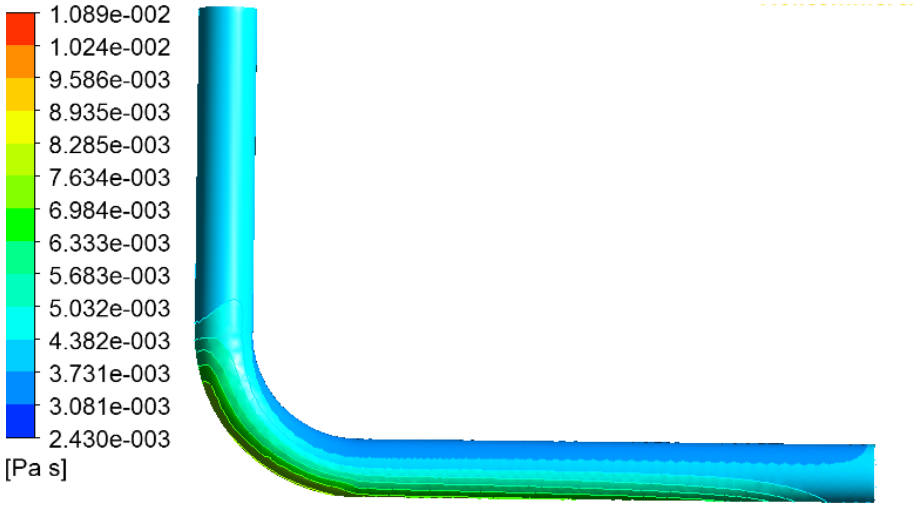

(a) Solid viscosity based on the Roscoe-Brinkmann correlation [94]

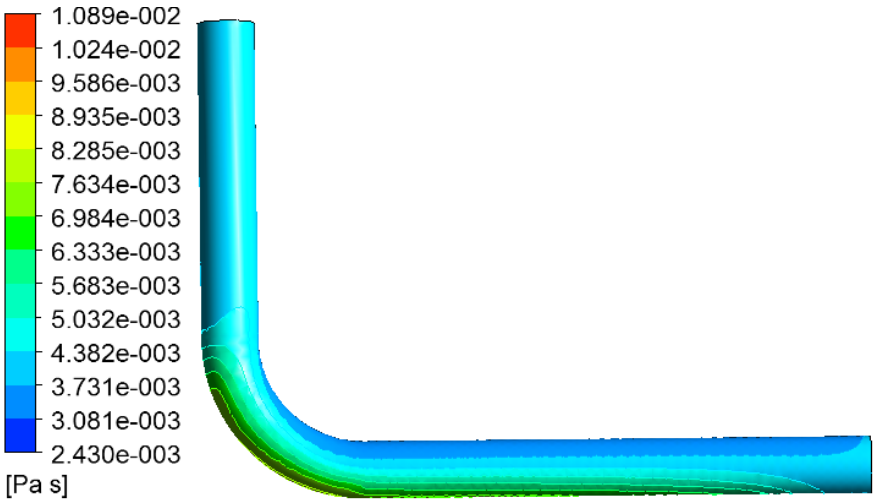

(b) Solid viscosity based on the expression derived by Krieger-Dougherty [95]

Figure 6.20: *Contour plots of the suspension viscosity in the near wall region. Contours for expressions derived by Roscoe-Brinkmann [94] and Krieger-Dougherty [95].*

velocity in the range of 0.1 - 0.4 m/s. The bed thickness from the results are presented in Figure 6.21 and compared with the data from the simulations with the viscosity expression included. It is clear that the viscosity has an important effect on the bed thickness, thus it is important to use a viscosity which is in accordance with the suspension viscosity found from experiments.

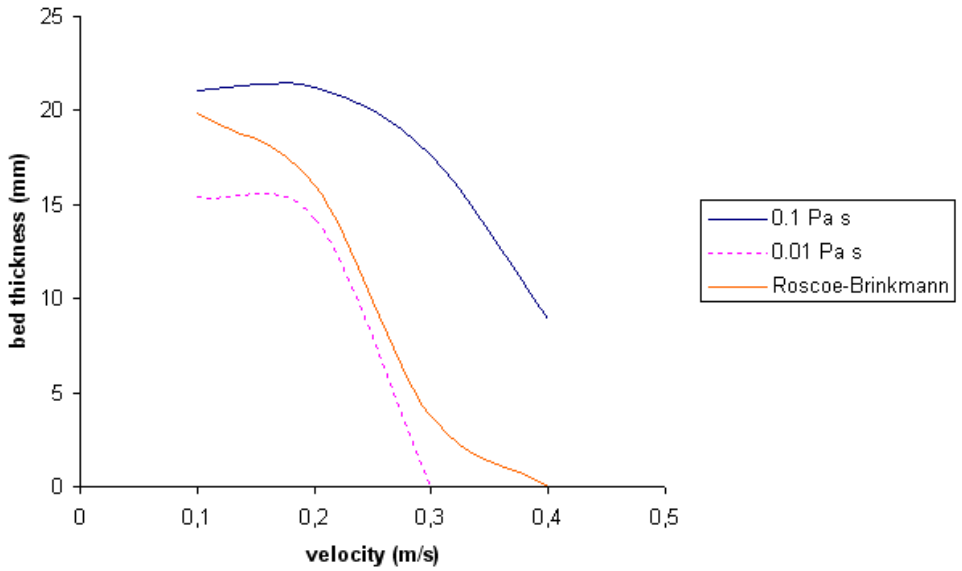

Figure 6.21: *Bed height as a function of hydrate volume fraction for different values of the solid viscosity is compared.*

A midline cross-section showing the continuous fluid velocity is given in Figure 6.22 for a mean flow velocity of 0.2 m/s. The fluid velocity magnitude in the bed is much lower than in the "clear" part of the fluid. This is due to the high solid phase viscosity in the bed. At the wall the velocity is zero due to the no-slip boundary condition at the wall which assumes that the velocity at the wall is zero.

6.5.2 Effect of particle size

The particle size was set to be dependent of flow parameters and their cohesive properties according to the work by Mühle [97]. The particle size as a function of velocity was presented in Chapter 5.5. A sensitivity was done to study the effect of the particle size. Simulations were done with basis in the solids pressure model, 0.2 m/s mean flow velocity and the Roscoe-Brinkmann correlation [94] for the solid viscosity. Particle sizes in the range 170 - 330 μm were used.

The bed thickness versus particle diameter is presented in Figure 6.23. It is clear that the particle size affects the thickness of the bed. The thickness of the formed bed increases with increasing particle size. This was expected

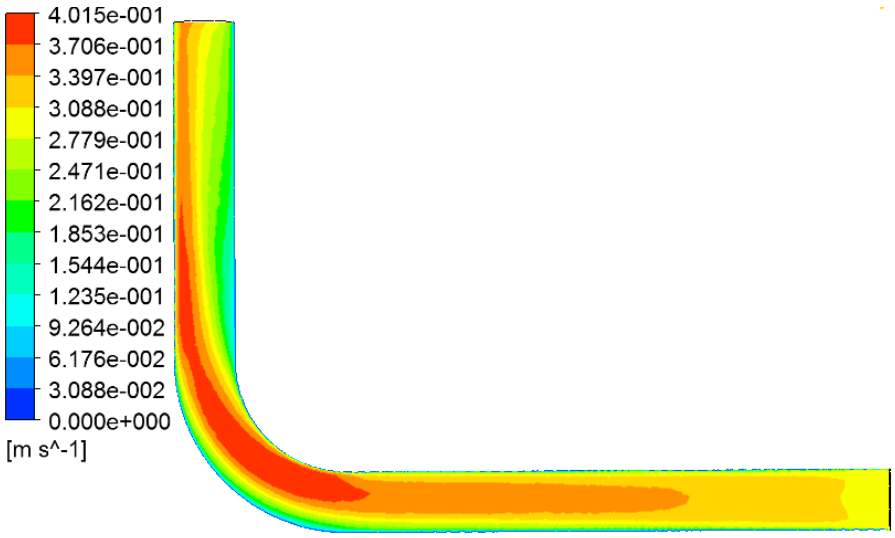

(a) A midline cross-sectional contour of the continuous phase velocity

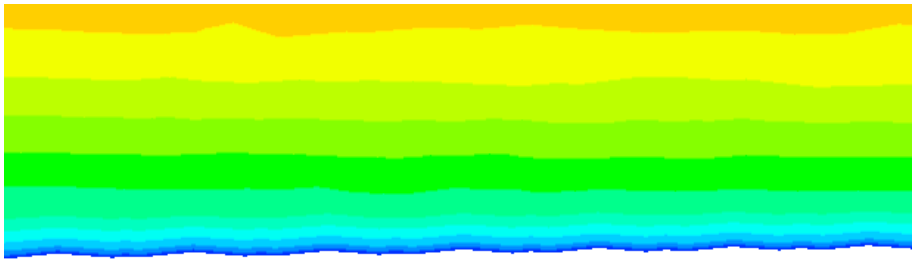

(b) A close-up of the bottom part of the pipe in the horizontal region showing the continuous phase velocity in the near-wall region.

Figure 6.22: *Contours showing the continuous phase velocity on a midline cross-section. It is clear that the velocity in the bed is lower than the velocity in the "clear" part of the fluid.*

since the terminal settling velocity of the particles in the gravity field increases with increasing size.

The literature on aggregation and breakage of cohesive particles shows that mean particle size in the system is strongly dependent on the shear rate [101, 102] which is related to the turbulent energy dissipation rate [103]. Contour plot of the dissipation rate for a mean flow velocity of 0.1 m/s is presented in Figure 6.24. It can be seen from the plot that the regions with the most intensive dissipation are in the inner part of the bends, shifting to

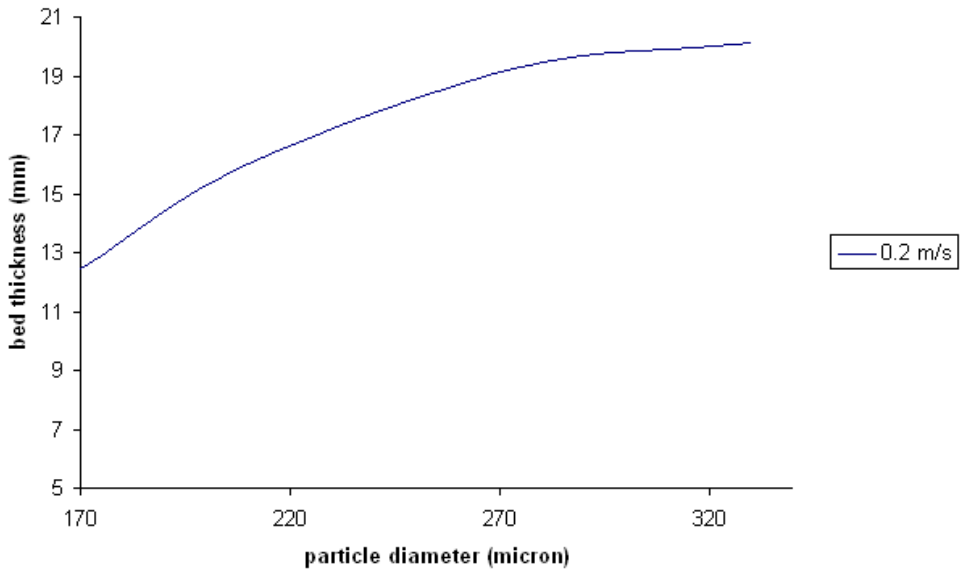

Figure 6.23: *The dependency of particle size on bed formation is shown. The particle diameter was in the range 170 to 330 μm. The mean flow velocity was 0.2 m/s.*

the outside just downstream of the bends, corresponding with the velocity maximum changing location. Thus it is expected that the mean particle size would be at the minimum due to the breakage [104] while the quiescent regions are aggregation-dominated.

6.5.3 Concentration gradients

From the experiments it was seen a difference in the concentration gradient between the settled bed and the homogeneous fluid dependent on the mean flow velocity. At low mean flow velocities (fluid still flowing) it was observed a sharp concentration gradient between the upper part of the bed and the bulk fluid. Figure 6.12 presents a photograph of a stable hydrate bed formed at a flow velocity of 0.1 m/s. It can be seen from the photograph that the flow is stratified into two zones of very different particulate phase concentration.

At higher mean flow velocities this "sharpness" was not seen since the homogeneous suspension was less dilute. Figure 6.11 shows this not so sharp region for a mean flow velocity of 0.28 m/s.

It was investigated in this work if CFX was able to predict a steeper con-

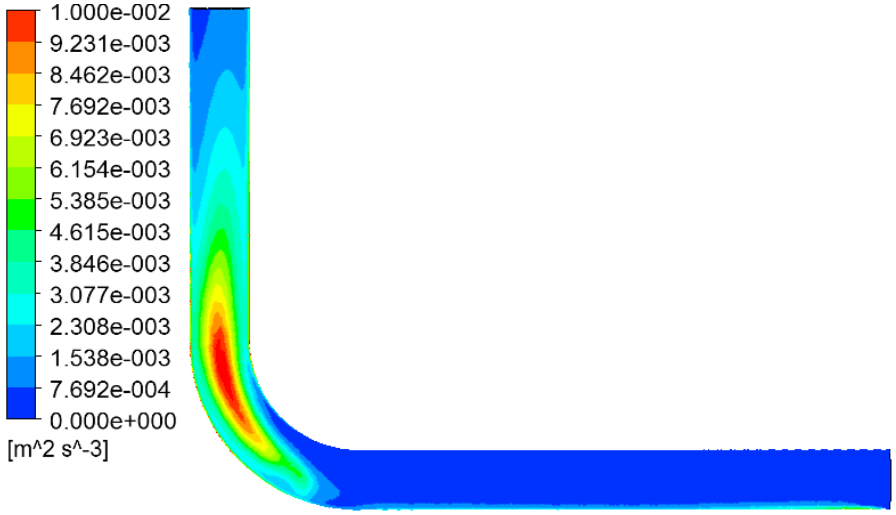

Figure 6.24: *Contour plot of the turbulent kinetic energy dissipation rate on the a midline cross-section. Hydrate volume fraction: 0.05, mean flow velocity: 0.1 m/s, hydrate particle size: 330 μm.*

centration gradient at lower mean flow velocities. The concentration in the near wall region relative to the pipe diameter as a function of the mean flow velocity was found. Simulations were done using mean flow velocities in the range 0.1 - 0.3 m/s. The particles were set to be dependent on the flow velocity and the solid viscosity to follow the Roscoe-Brinkmann [94] correlation. The results are presented in Figure 6.25.

Figure 6.25 shows that CFX is not able to predict the sharp concentration gradient as was observed during experiment. A possible reason for this can be within the multiphase model. The Eulerian-Eulerian model does not track the interface between the fluids, it only tracks the contours of the volume fraction. Another possible reason for the poor agreement with experimental observations at low flow velocities can be due to the grid. To get sharper interfaces between the bed and the homogeneous suspension the grid near the interface boundary could be refined. A grid refinement in the interface was done to see if it affected the predicted concentration gradient. The results from the refined grid case showed no improvement of the interphase boundary prediction. An even more refined grid was not simulated due to limited computational power.

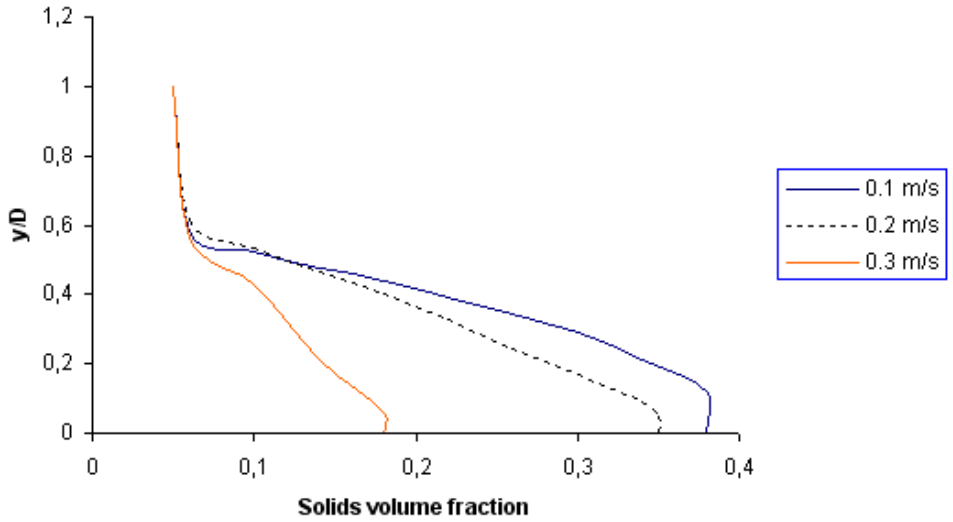

Figure 6.25: *Hydrate volume fraction as a function of dimensionless vertical coordinate. Mean flow velocities 0.1 - 0.3 m/s.*

6.5.4 Wall boundary conditions

The wall boundary conditions used in this study is the "no-slip" condition for both phases, which means that the velocity at the wall is zero. This is justified by the fact that particles close to a surface do not move along with a flow when adhesion is stronger than cohesion. An alternative approach is to set the wall boundary phase for the solid phase to "free-slip". In this case the shear stress at the wall is zero, and the velocity of the fluid near the wall is not retarded by wall friction effects. The no-slip is the most physically correct as in reality the particles will not slide freely on the wall, but rather do some momentum exchange with it. The most ideal would be to include an expression for the "partial slip", but this is very complex and thus not suitable for this model. The case of using free-slip boundary condition would present very dilute suspensions with hard spherical particles.

The effect of the wall boundary condition was studied. The same set up as for the solids pressure model was used. The wall boundary condition for the solid phase was changed from no-slip to free-slip. Simulations were done with mean flow velocities in the range 0.1 - 0.4 m/s. Contours of the hydrate volume fraction at the wall is given in Figure 6.26 for the free-slip sensitivity.

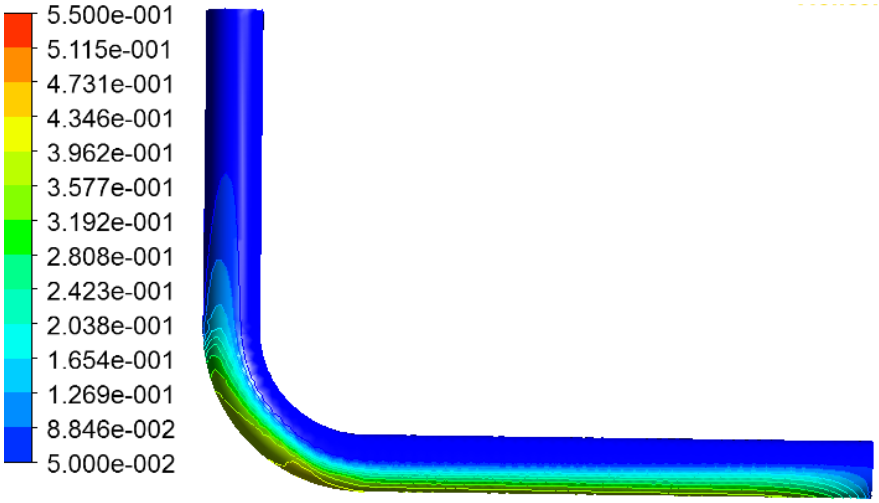

(a) Mean flow velocity 0.1 m/s

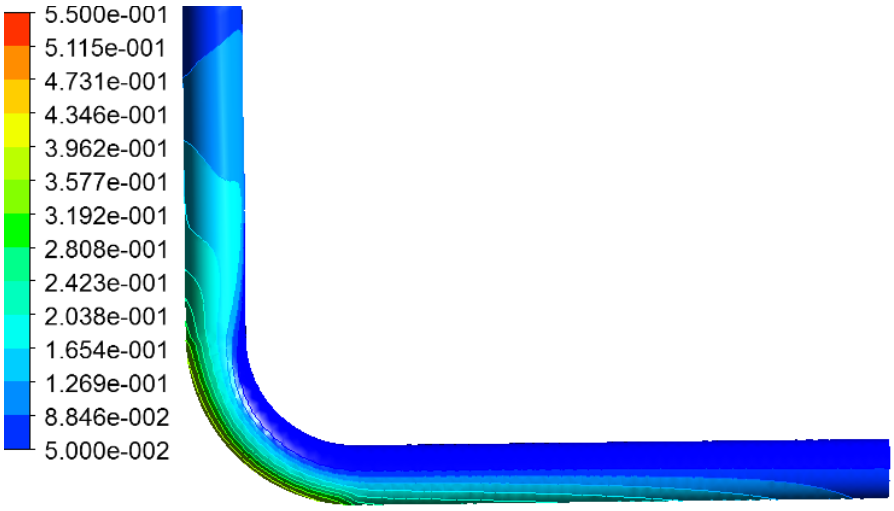

(b) Mean flow velocity 0.2 m/s

Figure 6.26: *Contour plots of the hydrate volume fraction in the near wall region for solids pressure simulations using the "free-slip" wall boundary condition for the dispersed phase. As for the simulations using the "no-slip" condition for both phases, the hydrate volume fraction at the wall decreases at increasing velocities. The overall bed is thinner compared to simulations using the no-slip condition.*

The hydrate volume fraction in the near-wall region using the free-slip boundary condition is dramatically reduced compared to similar simulations with the no-slip condition. The maximum hydrate volume fraction in the bed is

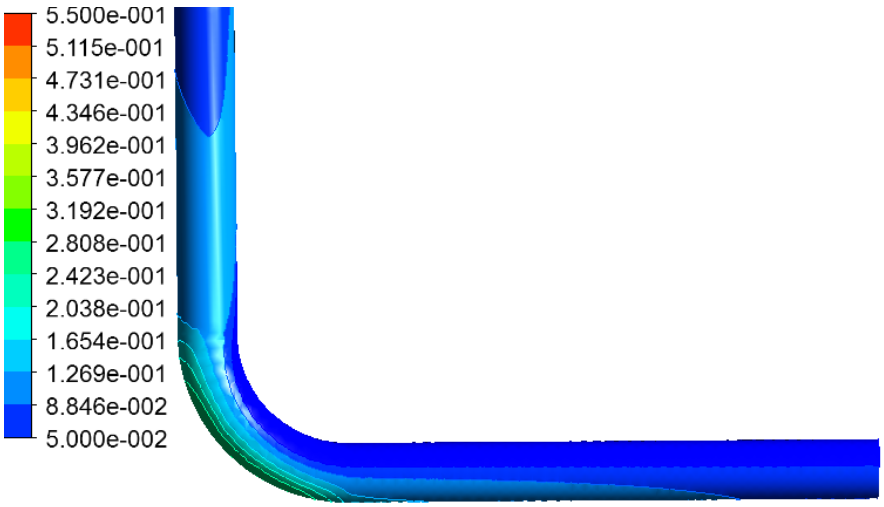

(c) Mean flow velocity 0.3 m/s

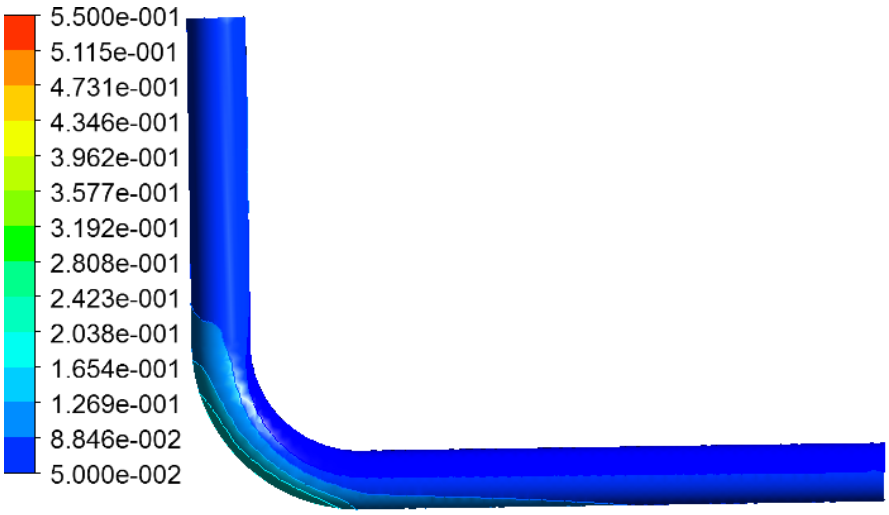

(d) Mean flow velocity 0.4 m/s

Figure 6.26: *Contour plots of the hydrate volume fraction in the near wall region for Solids pressure simulations using the "free-slip" wall boundary condition for the dispersed phase. As for the simulations using the "no-slip" condition for both phases, the hydrate volume fraction at the wall decreases at increasing velocities. The overall bed is thinner compared to simulations using the no-slip condition.*

in the range 0.2 - 0.3 compared to 0.4 - 0.5 for the no-slip condition. This sensitivity shows that being able to model the flow near the wall is very important to be able to predict the flow behavior.

The bed thickness as a function of the mean flow velocity using the free-slip boundary condition is given in Figure 6.27. The wall thickness is compared to similar simulations using the no-slip boundary condition for both phases.

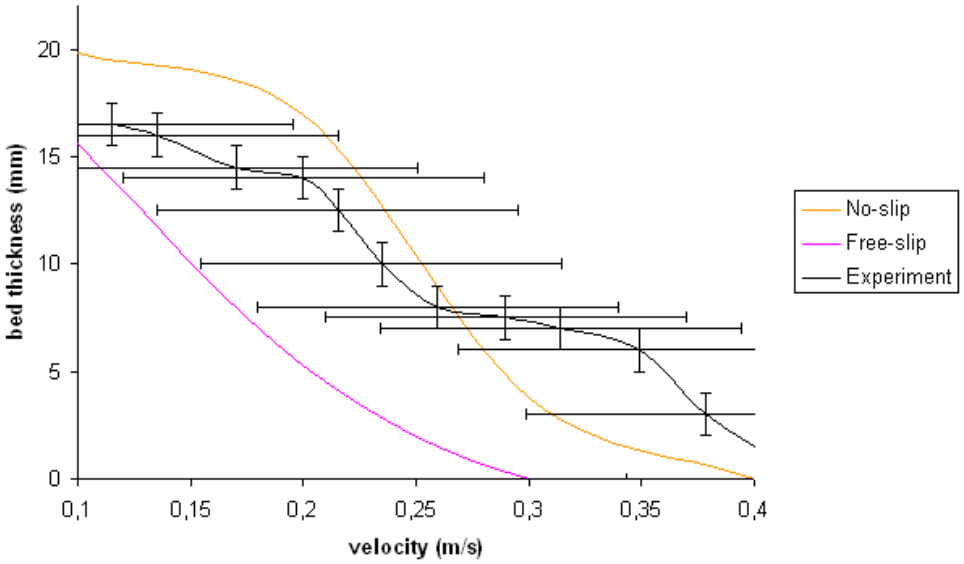

Figure 6.27: *Comparison of the hydrate bed thickness in the free-slip simulations compared to results from simulations using the no-slip condition for both phases.*

6.5.5 Effect of the turbulent dispersion force

As described above there was a difference in the set-up between the models in CFX and STAR-CD. In STAR-CD the turbulent dispersion force was used, while in this work it was not. The turbulent dispersion force results in additional dispersion of phases from high volume fraction regions to low volume fraction regions due to turbulent fluctuations. This is caused by the combined action of turbulent eddies and interphase drag. In the simulations the dispersed particles get caught up in continuous phase turbulent eddies, and are transported by the effect of interphase drag.

A sensitivity was done to see the effect of the turbulent dispersion force on the bed formation. Simulations were performed with mean flow velocities in the range 0.1 - 0.4 m/s. The results showed that even at 0.1 m/s the hydrate bed was dispersed in the continuous fluid. This is shown in Figure 6.28.

The sensitivity was started with initial values from a simulation without the dispersion force enabled. The maximum hydrate volume fraction in the pipe was decreased from approximately 0.5 to 0.15. The simulations for the larger mean velocity showed the same tendency.

In Chapter 6.3 the time of bed formation was discussed. The bed formation predicted by the numerical model did not correspond to what was observed during experiments. Simulations with a total time of 80 s were performed to investigate whether using the turbulent dispersion force would predict the bed formation in accordance with experiments. The simulations with the turbulent dispersion force did predict the same rapid bed growth as was seen in earlier simulations without the turbulent dispersion force.

Balakin [1] reported on minor differences between similar simulations with and without the turbulence dispersion force. A possible reason for the deviations between CFX and STAR-CD has not been found. Both softwares use the "Favre Averaged Drag Model" which has shown a wide range of universality.

One possible reason for the prediction of the small bed when using the turbulent dispersion force is caused by an overprediction of the turbulent dispersion force. This can be due to the turbulence model. The $k - \epsilon$ model tends to over-predict k by a factor of 2 or 3. This is usually not a problem since ϵ is often also over-predicted but it is known to cause too much turbulent dispersion.

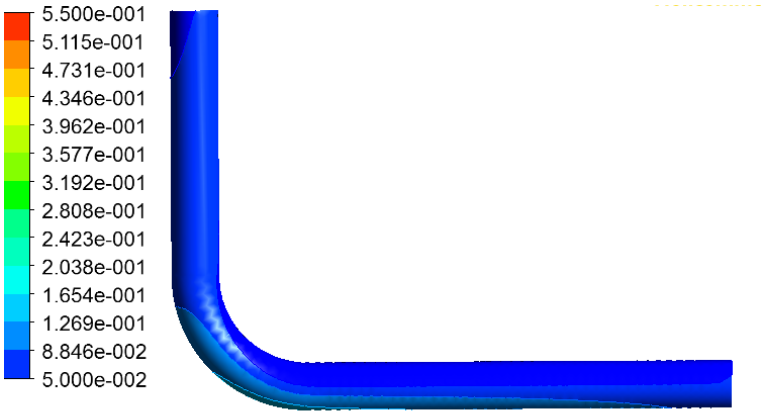

Figure 6.28: *Contour presenting the hydrate volume fraction in the near wall region using the turbulent dispersion force. Mean flow velocity 0.1 m/s.*

Chapter 7

Conclusion

Formation of gas hydrates in process equipment and pipelines is a major scientific problem. Even though much research has been done on hydrate formation and growth not all mechanisms are yet still well known. The main goal of this master thesis was to study the formation of hydrates with use of the commercial CFD software ANSYS CFX. This thesis aimed to supplement the CFD simulations done using STAR-CD with simulations using ANSYS CFX for purposes of comparison and clearer interpretation of the physics of bed formation.

A three-dimensional, transient Eulerian-Eulerian two-fluid model was created in order to study the deposition of hydrates in a horizontal pipe. The results from the simulations were compared with results conducted from experiments and simulations using STAR-CD. Simulations were performed in the flow regime whereby hydrate deposition takes place using two different particle collision models. Sensitivity studies were performed for the clarification of the effects of the mean particle size, solids viscosity and different model set-up on the model outcome.

The numerical model was able to predict hydrate bed formation within the same flow regime as was observed experimentally. Simulations were done both using the kinetic theory of granular flow and Gidaspows solids pressure model. For the kinetic theory model the coupling between the pressure force on the solid at high packing fractions is not fully linearized with respect to changes in volume fraction. This gave poor convergence. The bed thickness as a function of the mean flow velocity predicted by the solids pressure model were in agreement within the experimental uncertainties from the experiment.

Sensitivity studies of the model were done for the clarification of the effects of the mean particle size, solid viscosity and boundary conditions. It was found

that the use of a particle size, which is independent of the mean flow velocity, would lead to quantitatively incorrect results. The use of a constant viscosity for the solid phase led to incorrect results for the dense phase regions. The wall boundary condition was changed from "no-slip" to "free-slip" which gave a significant decrease of the volume fraction of the dispersed phase.

The results obtained from the numerical study in this thesis were compared to similar simulations performed by the use of the commercial software STAR-CD. The results by the two softwares were in qualitatively agreement, but the results obtained by STAR-CD were generally in better agreement with the results from the experiment. The difference in results between the solvers can be explained by different geometry, grid, solver, discretization technique and model set-up.

CDF has growed to become a powerful tool in engineering and research and its importance will further grow as the computer resources increase and the development of more complex numerical schemes. In general, it is important to compare simulations between software packages to destil out which flow features are due to the numerical techniques and which can be assigned to the physics of the system.

The use of CFD to predict hydrate formation and behavior in a flow system can help improving our knowledge and be used as a tool in e.g the oil and gas industry to predict if the process can operate safely in the hydrate formation region. One limitation of the models today is the lack of experimental results for hydrate formation and growth in high pressure flow loops. It is important with extensive validation of the models to ensure their performance. Small changes in the physical process can lead to different conditions for hydrate growth. Enhanced robustness and prediction capabilities of the models can contribute to the change in philosophy from hydrate inhibition to risk management in the industry.

Nomenclature

$A_{\alpha\beta}$	interfacial area density	1/m
A_s	area betweeen layers	m^2
c	compaction modulus	
C_D	drag coefficient	
$C_u, C_{E1}, C_{E2}, \delta_k, \delta_t$	constants	
D	diameter	m
D_d	drag force	N/m^3
$\bar{D_n}$	mean particle diameter	m
e	coefficient for restitution for solid-solid collisions	
F_s	force	N
g_0	radial distribution function	
G_0	reference elasticity modulus	
$G(\phi_s)$	elasticity modulus	
K	turbulent kinetic energy	m^2/s^2
L	length	m
M	mass	kg
M_{omc}	momentum flux	N/m^2
p	pressure	Pa
P_k	generation of turbulent kinetic energy	m^2/s^2
$Pr_{\alpha\beta}$	fluid Prandtl number	
Re	Reynolds number	
$Re_{\alpha\beta}$	particle Reynolds number	
St_V	Stokes number	
t	time	s
u	local velocity	m/s
u^+	near wall veolcity	m/s
u_τ	friction velocity	m/s
v	velocity	m/s
$\bar{v}$	average velocity	m/s
V	volume	m^3
V_t	kinematic eddy viscosity	Pa s/ρ
x, y, z	Cartesian coordinates	m
y^+	dimensionless distance from the wall	

Greek letters

γ	shear rate	1/s
ϵ	turbulent energy dissipation rate	m^2/s^3
ζ_s	solids bulk viscosity	Pa s
κ	von Karman constant	
μ	viscosity	Pa s
μ_s	solids shear viscosity	Pa s
μ_t	turbulent viscosity	Pa s
π_{mom}	momentum coupling parameter	
ρ	density	kg/m^3
$\bar{\rho}$	bulk density	kg/m^3
σ	turbulent Prandtl number	
τ	shear stress	Pa
τ_c	average time between particle-particle collisions	s
τ_{sij}	collisional solid stress tensor	Pa
τ_v	momentum response time	s
ϕ	volume fraction	
ωn	standard deviation	

Subscripts

α	phase alpha
β	phase beta
c	continuous
d	dispersed
h	hydrate
l	liquid
m	mixture
max	maximum
sm	settled bed
$susp$	suspension
t	terminal
w	wall

Bibliography

[1] B. V. Balakin, A. C. Hoffmann, and P. Kosinski, "Computational fluid dynamic model for deposition of adhesive particles in a pipeline.." Submitted to Chemical Engineering Science, 2010.

[2] E. Sloan, *Clathrate hydrates of natural gases*. Marcel Dekker, 1998.

[3] E. D. Sloan, "Clathrate hydrates: The other common solid water phase," *Industrial and egineering Chemistry Research*, vol. 39, pp. 3123–3129, 2000.

[4] B. V. Balakin, H. Pedersen, Z. Kilinc, A. C. Hoffmann, and P. Kosinski, "Turbulent flow of freon r11 hydrate slurry," *Journal of Petroleum Science and Engineering*, vol. 70, pp. 177–182, 2008.

[5] J. J. Carroll, *Natural Gas Hydrates. A Guide for Engineers*. Gulf Professional Publishing, 2003.

[6] P. Atkins and J. Paula, *Atkins' Physical Chemistry*. Oxford University Press Inc., seventh ed., 2002.

[7] M. von Stackelberg *Naturwissenschaften*, vol. 36, pp. 327,359, 1949.

[8] G. A. Jeffrey, *Inclusion Compounds*, vol. 1. Acad. Press., 1984.

[9] J. P. Long and E. D. Sloan, "Hydrates in the ocean and evidence for the location of hydrate formation," *Internation Journal of Thermophysics*, vol. 17, pp. 1–13, 1996.

[10] B. Kvamme, "A unified nucleation theory for the kinetics of hydrate forrmation," *Annals of the New York Academy of Sciences*, vol. 912, pp. 496–501, 2000.

[11] B. Kvamme, "Initiation and growth of hydrate," in *4th International Conference on Natural Gas Hydrate*, 2002.

[12] J. Long, *Gas Hydrate Formation Mechanism and its Kinetic Inhibition*. PhD thesis, Colorado School of Mines, 1994.

[13] R. L. Christiansen and E. D. Sloan, "Journal in proc. first international conference on natural gas hydrates," *Ann. N. Y. Acad. Science, New Paltz, NY*, June 13-16, 1993.

[14] L. A. Baez and P. Clancy, "Journal in proc. first international conference on gas hydrates," *Ann. N. Y. Acad. Science*, vol. 715, 1994.

[15] R. Radhakrishnan and B. L. Trout, "A new approach for studying nucleation phenomena using molecular simulations: Application to co2 hydrate clathrates," *Journal Chemistry Physics*, vol. 117, 2002.

[16] C. Moon, P. C. Taylor, and P. M. Rodger, "Molecular dynamics study of gas hydrate formation," *Journal of American Chemical Society*, vol. 125, pp. 4706–4707, 2003.

[17] Y. Makogon, T. Makogon, and S. Holditch, "Gas hydrate formation and dissociation with thermodynamic and kinetics inhibitors," in *SPE annual Technical Conference and Exhibition*, (Houston), 3- 6 October 1999.

[18] E. G. Hammerschmidt, "Formation of gas hydrates in natural gas transmission lines," *Industrial and Engineering Chemistry*, vol. 26, no. 8, pp. 851–855, 1934.

[19] L. Bergfløt, L. H. Gjertsen, J. Sjøblom, H. Kallevik, and G. Øye, "Chemical influence on the formation, agglomeration, and natural transportability of gas hydrates. a multivariate component analysis," *Journal of Dispersion Science and Technology*, vol. 25, no. 3, pp. 355–365, 2004.

[20] B. F. Baugh, "Testing and evaluation of coild tubing methods to remove blockages from long offset subsea pipelines," in *OTC 8524*, May 1997.

[21] K. Minami, "Ensuring flow and production in deepwater environments," in *OTC 11035*, May 1999.

[22] P. P. Lang, R. M. Rainey, and C. H. Bankstons, "Mensa project: System design and operation," in *OTC 8577*, May 1998.

[23] D. Lysne, "Hydrate plug dissociation by pressure reduction," *International conference on natural gas hydrates*, vol. 715, pp. 514–517, 1994.

[24] J. D. Lee, H. Wu, and P. Englezos, "Cationic starches as gas hydrate kinetic inhibitors," *Chemical Engineering Science*, vol. 62, no. 23, pp. 6548–6555, 2007.

[25] M. A. Kelland, "History of the development of low dosage hydrate inhibitors," *Energy & Fuels*, vol. 20, no. 3, pp. 825–847, 2006.

[26] Z. Huo, E. Freer, M. Lamar, B. Sannigrahi, D. M. Knauss, and E. D. Sloan jr., "Hydrate plug prevention by anti-agglomeration," *Chemicla Engineering Science*, vol. 56, no. 17, pp. 4979–4991, 2001.

[27] S. Høiland, K. M. Askvik, P. Fotland, E. Alagic, T. Barth, and F. Fadnes, "Wettability of freon hydrates in crude oil/brine emulsions," *Journal of Colloid and Interface Science*, vol. 287, no. 1, pp. 217–225, 2005.

[28] S. Høiland, A. E. Borgund, T. Barth, P. Fotland, and K. M. Askvik, "Wettability of freon hydrates in crude oil/brine emulsions: the effect of chemical additives," *Proceedings of the fifth International Conference on Gas Hydrates, Trondheim, Norway*, 2005.

[29] R. L. Christiansen and E. D. Sloan jr., "Mechanisms and kinetics of hydrate formation," *Natural Gas Hydrates*, vol. 715, pp. 283–305, 1994.

[30] J. P. Lederhos, J. P. Long, A. Sum, R. L. Christiansen, and E. D. Sloan jr., "Effective kinetic inhibitors for natural gas hydrates," *Chemical Engineering Science*, vol. 51, no. 8, pp. 1221–1229, 1996.

[31] L. Del Villano, R. Kommedal, and M. A. Kelland, "Class of kinetic hydrate inhibitors with good biodegradability," *Energy & Fuels*, vol. 22, no. 5, pp. 3143–3149, 2008.

[32] M. Arjmandi, D. Leinweber, and K. Allan, "Development of a new class of green kinetic hydrate inhibitors," *19th International Oil Field Chemistry Stymposium, Geilo, Norway*, March 2008.

[33] F. H. Fadnes, "Natural hydrate inhibiting components in crude oils," *Fluid Phase Equilibria*, vol. 117, no. 1-2, pp. 825–847, 1996.

[34] C. Gaillard, J. P. Monfort, and J. L. Peytavy, "Investigation of methane hydrate formation in a recirculating flow loop: Modeling of the kinetics and tests of efficiency of chemical additives on hydrate inhibition," *Oil & Gas Science and Technology*, vol. 54, no. 3, pp. 365–374, 1999.

[35] L. Bergfløtdt, *Influence of crude oil based surface active components and synthetic surfactants on gas hydrate behaviour*. PhD thesis, Department of Chemistry, University of Bergen, 2001.

[36] E. M. Leporcher, J. L. Peytavy, Y. Mollier, J. Sjoblom, and C. Labes-Carrier, "Multiphase transportation: hydrate plugging prevention

through crude oil natural surfactants," *Society of petroleum engineers*, vol. Paper 49172, 1998.

[37] A. Sinquin, X. Bredzinsky, and V. Beunat, "Kinetic of hydrates formation: Influence of crude oils," *Society of Petroleum Engineers*, vol. Paper 71543, 1998.

[38] P. Fotland and K. M. Askvik, "Some aspects of hydrate formation and wetting," *Journal of Colloid and Interface Science*, vol. 321, no. 1, pp. 130–141, 2008.

[39] A. Sinquin, D. Arla, J. L. Peytavy, C. Prioux, P. Glenat, and C. Dicharry, "Gas hydrate formation and transport in an acidic crude oil: Influence of salt and ph," *Energy & Fuels*, vol. 22, no. 2, pp. 721–728, 2008.

[40] J. Connan, *Advances in Petroleum Geochemistry (J. Brooks and D. Welte, eds.)*, ch. Biodegradation of Crude Oils in Reservoirs, pp. 299–335. Academic Press, London, 1984.

[41] E. J. McKenna and R. E. Kallio, "The biology of hydrocarbons," *Annual Review of Microbiology*, vol. 19, pp. 183–208, 1965.

[42] B. Beauchamp, "Natural gas hydrates: myths, facts and issues," *C. R. Geoscience*, vol. 336, pp. 751–765, 2004.

[43] C. Crowe, M. Sommerfeld, and Y. Tsuji, *Multiphase Flows With Droplets and Particles*. CRC PRESS, 1998.

[44] W. L. McCabe, J. C. Smith, and P. Harriott, *Unit Operations of Chemical Engineering*. McGraw-Hill, 2005.

[45] R. B. Munson, F. D. Young, and H. T. Okiishi, *Fundamentals of fluid mechanics*. John Wiley & Sons, Inc., third ed., 2003.

[46] O. Reynolds *Phil. Trans Royal Soc. London, Ser. A*, vol. 174, 1883.

[47] M. Ishii, *Thermo-Fluid Dynamics Theory of Two-Phase Flow*. Eyrolles Paris, 1975.

[48] J. D. Anderson, *Computational Fluid Dynamics, The Basics with Applications*. McGraw-Hill, 1995.

[49] W. Wang, S. Fan, D. Liang, and X. Yang, "Experimental study on flow characters of CH_3CCI_2F hydrate slurry," *International Journal of Refrigeration*, vol. 31, no. 3, pp. 371–378, 2008.

[50] M. Darbouret, M. Cournil, and J.-M. Herri, "Rheological study of tbab hydrate slurries as secondary two-phase refrigerants," *International Journal of refrigeration*, vol. 28, pp. 663–671, August 2005.

[51] A. Sinquin, T. Palermo, and Y. Peysson, "Rheological and flow properties of gas hydrate suspensions," *Oil & Gas Science and Technology*, vol. 59, no. 1, pp. 41–58, 2004.

[52] B. V. Balakin, A. C. Hoffmann, and P. Kosinski, "Computational fluid dynamic model of gas hydrate deposition in a turbulent flow," in *Gas hydrates resources development*, 17-18 November 2009.

[53] D. Newitt and J. Richardson, "Hydraulic conveying of solids in horizontal pipes," *Trans. Instn. Chem. Engng*, vol. 33a, pp. 93–113, 1955.

[54] P. Doron and D. Barnea, "A three-layer model for solid-liquid flow in horizontal pipes," *Int. J. Multiphase Flow*, vol. 19, pp. 1029–1043, 1993.

[55] A. Alajbegovic, *Phase Distribution and Turbulence Structure for Solid/Fluid Upflow in a Pipe.* PhD thesis, Rensselaer Polytechnic Institute, Troy New York, 1997.

[56] M. Muste and V. Patel, "Velocity profiles for particles and liquid in open-channel flow with suspended sediment," *Journal of Hydraulic Engineering*, vol. 123, no. 9, pp. 742–751, 1997.

[57] A. Taniere, B. Oesterle, and J. Monnier, "On the behaviour of solid particles in a horizontal boundary layer with turbulence and saltation effects," *Experiments in Fluids*, vol. 23, no. 6, pp. 463–471, 1997.

[58] R. Durand, "Basic relationships of the transportation of solids in pipes: Experimental research," in *Proceedings of the 5th Congress, International Association of Hydraulic Research*, 1953.

[59] E. J. Wasp, T. C. Aude, J. P. Kenny, R. H. Seiter, and R. B. Jaques, "Deposition velocities, transition velocities and spatial distribution of solids in slurry pipelines," in *Proceedings of the 1st International Conference on the Hydraulic Transport of Solids in Pipes (Hydrotransport 1)* (U. BHRA Fluid Engineering: Cranfield, ed.), no. Paper H4, pp. 53–76, 1970.

[60] C. Shook and S. Daniel, "A variable density model of the pipeline," *Can. J. Chem. Eng.*, vol. 47, no. 2, pp. 196–200, 1969.

[61] A. R. Oroskar and R. M. Turian, "The critical velocity in pipeline flow of slurries," *AIChE Journal*, vol. 26, pp. 551–558, 1980.

[62] K. C. Wilson and F. J. Pugh, "Dispersive-force modeling of turbulent suspension in heterogeneous slurry flow," *Can. J. Chem. Eng.*, vol. 66, pp. 721–727, 1988.

[63] K. C. Wilson, "A unified physical-based analysis of solid-liquid pipeline flow," in *Proceedings of the 4th International Conference of Hydraulic Transport of Solids in pipes (Hydrotransport 4)* (U. BHRA Fluid Engineering: Cranfield, ed.), no. Paper A1, pp. 1–16, 1976.

[64] R. G. Gillies, C. A. Shook, and K. C. Wilson, "An improved two-layer model for horizontal slurry pipeline flow," *Can. J. Chem. Eng.*, vol. 69, pp. 173–178, 1991.

[65] R. G. Gillies and C. A. Shook, "A concentration distribution of sand slurries in horizontal pipe flow," *Part. Sci. Technol*, vol. 12, pp. 45–69, 1994.

[66] R. G. Gillies and C. A. Shook, "A modelling high concentration slurry flows," *Can. J. Chem. Eng.*, vol. 78, pp. 709–716, 2000.

[67] R. G. Gillies, C. A. Shook, and J. Xu, "Modelling heterogeneous slurry flows at high velocities," *Can. J. Chem. Eng.*, vol. 82, pp. 1060–1065, 2004.

[68] K. Ekambara, R. S. Sanders, K. Nandakumar, and J. H. Masliyah, "Hyrodynamic simulation of horizontal slurry pipeline flow using ansys-cfx," *Ind. Eng. Chem. Re*, vol. 48, pp. 8159 – 8171, 2009.

[69] R. Chein and W. Liao, "Analysis of particle-wall interaction during particle free fall," *Journal of Colloid and Interface Science*, vol. 288, no. 104, 2005.

[70] M. Rashidi, "Particle-turbulence interaction in a boundary layer," *International Journal of Multiphase Flow*, vol. 16, no. 935, 1990.

[71] M. Sommerfeld, "Modeling of particle-wall collisions in condined gas-particle flows," *Multiphase Flow*, vol. 18, no. 905, 1992.

[72] J. H. Vincent, *Aerosol Science for industrial Hygienists.* Elsevier Science Inc., New York, 1st ed., 1995.

[73] C. Yang, "Kinetics of particle transport to a solid surface from an impinging jet under surface and external force fields," *Journal Colloid and Interface Science*, vol. 208, no. 226, 1998.

[74] B. V. Derjaguin and L. Landau, "Theory of the stability of strongly charged lyophobic sols and of the adhesion of strongly charged particles in solutions of electrolytes," *Acta Physiocochim*, vol. 14, pp. 633–662, 1941.

[75] E. J. Verwey and J. T. G. Overbeek, *Theory of stability of Lyophobic Colloids*. Elsevier, Amsterdam, 1948.

[76] E. Jassim, M. A. Abdi, and Y. Muzychka, "A cfd-based model to locate flow restriction induced hydrate deposition in pipelines," in *In Offshore Technology Conference Proceedings*, 2008.

[77] B. P. B. Hoomans, J. A. M. Kuipers, W. J. Briels, and W. P. M. van Swaaij, "Discrete particle simulation of bubble and slug formation in a two-dimensional gas-fluidised bed: a hard sphere approach," *Chem. Eng. Sci*, vol. 51, no. 99, pp. 99–108, 1996.

[78] P. Kosinski and A. C. Hoffmann, "An extension of the hard-sphere particle-particle collision model to study agglomeration," *Chemical Engineering Science*, vol. 65, pp. 3231–3239, 2010.

[79] A. Castellanos, J. M. Valverde, and M. A. S. Quintanilla, "Aggregation and sedimentation in gas-fluidized beds of cohesive powders," *Physical Review. E*, vol. 64, no. 4, 2001.

[80] H. Lu, Z. Shen, J. Ding, L. Xiang, and H. Liu, "Numerical simulation of bubble and particles motions in a bubbling fluidized bed using direct simulation monte-carlo method," *Powder Technology*, vol. 169, no. 159, 2006.

[81] H. Lu, Y. Zhao, J. Ding, D. Gidaspow, and L. Wei, "Investigation of mixing/segregation of particles in gas-solid fluidized beds," *Chemical Engineering Science*, vol. 62, no. 301, 2007.

[82] E. Helland, R. Occelli, and L. Tadrist, "Numerical study of cluster and particle rebound effects in a circulating fluidised bed," *Chemical Engineering Science*, vol. 60, no. 27, 2005.

[83] T. Mikami, H. Kamiya, and M. Horio, "Numerical simulation of cohesive powder behaviour in a fluidized bed," *Chemical Engineering Science*, vol. 53, no. 10, pp. 1927–1940, 1998.

[84] G. Lian, C. Thornton, and M. J. Adams, "Discrete particle simulation of agglomerate impact coalescence," *Chemical Engineering Science*, vol. 53, no. 19, pp. 3381–3391, 1998.

[85] I. S. . T. D. ANSYS, *ANSYS CFX - Solver Theory Guide*, 2009.

[86] L. I. Berge, L. H. Gjertsen, and D. Lysne, "Measured permeability and porosity of r11 hydrate plugs," *Chemical Engineering Science*, vol. 53, pp. 1631–1638, 1998.

[87] D. Pfleger, S. Gomes, N. Gilbert, and H. Wagner, "Hydrodynamic simulations of laboratory scale bubble columns fundamental studies of the eulerian-eulerian modelling approach.," *Chemical Engineering Science*, vol. 54, pp. 5091–5099, 1999.

[88] B. E. Launder and B. I. Sharma, "Application of the energy dissipation model of turbulence to the calculation of flow near a spinning disc," *Letters in Heat and Mass Transfer*, vol. 1, no. 2, pp. 131–138, 1974.

[89] C. Y. Wen and Y. H. Yu, "Mechanics of fluidization," *Chemical Engineering Progress*, vol. 62, pp. 100–111, 1966.

[90] D. Gidaspow, *Multiphase Flow and Fluidization: Continuum and Kinetic Theory Descriptions*. Academic Press, New York, 1994.

[91] S. Ergun, "Fluid flow through packed columns," *Chemical Engineering Progress*, vol. 28, pp. 89–94, 1952.

[92] B. V. Balakin, A. C. Hoffmann, and P. Kosinski, "Turbulent flow of hydrates in a pipeline of complex configuration." Preprint submitted to Elsevier, 2009.

[93] A. Hoffmann and H. Finkers, "A relation for the void fraction of randomly packed particle beds.," *Powder Technology*, vol. 82, pp. 197–202, 1995.

[94] W. Pabst, "Fundamental principles and applications of natural gas hydrates," *Nature*, vol. 426, pp. 353–363, 2004.

[95] I. Krieger and T. Dougherty, "A mechanism for non-newtonian flow in suspensions of rigid spheres," *Trans. SOc. Rheol.*, vol. 3, pp. 52–137, 1959.

[96] B. V. Balakin, A. C. Hoffmann, and P. Kosinski, "Population balance model for nucleation, growth, aggregation, and breakage of hydrate particles in turbulent flow.," *AIChE JOURNAL*, vol. 56, 2009.

[97] K. Mühle, *Floc stability in laminar and turbulent flow: Coagulation and Flocculation: Theory and Application (B. Dobias, Ed.), Surfactant Science Series*, vol. 47. Acad. Press., 1993.

[98] B. V. Balakin, A. C. Hoffmann, and P. Kosinski, "Determination of the upper boundary of a moving particle bed." Talk at University of Bergen, Apr., May 2010.

[99] H. Nicolai, B. Herzhaft, E. Hinch, L. Oger, and E. Guazelli, "Particle velocity fluctuations and hydrodynamic self-diffusion of sedimenting non-brownian spheres.," *Physics of Fluids*, vol. 1, pp. 12–23, 1995.

[100] P. Doron and D. Barnea, "Pressure drop and limit deposit velocity for solid liquid flow in pipes.," *Chemical Engineering Science*, vol. 50, pp. 1595–1604, 1995.

[101] M. Hounslow, R. Ryall, and V. Marshall, "A discretized population balance for nucleation, growth, and aggregation," *AICHE Journal*, vol. 34, pp. 1821–1832, 1988.

[102] L. Wang, D. Marchisio, R. Vigil, and R. Fox, "Cfd simulation of aggregation and breakage processes in laminar taylor-couette flow," *Journal of Colloid and Interface Science*, vol. 282, pp. 380–396, 2005.

[103] A. Heath, P. Bahri, P. Fawell, and J. Farrow, "Polymer flocculation of calcite: experimental results from turbulent pipe flow.," *AICHE Journal*, vol. 45, pp. 1284–1293, 2006.

[104] J. Herri, J. Pic, F. Gruy, and M. Cournil, "Methane hydrate crystallization mechanism from in-situ particle sizing.," *AICHE Journal*, vol. 45, pp. 590–602, 1999.